Iterative Coupled Shell/Tube Simulation of Waste Heat Boilers using Computational Multiphysics

by

Victor Guiguer

A thesis
presented to the University of Waterloo
in fulfillment of the
thesis requirement for the degree of
Master of Applied Science
in
Chemical Engineering

Waterloo, Ontario, Canada, 2019

© Victor Guiguer   2019

Examining Committee Membership

The following served on the Examining Committee for this thesis. The decision of the Examining Committee is by majority vote.

Supervisor: Nasser Mohieddin Abukhdeir
Associate Professor, Dept. of Chemical Engineering,
University of Waterloo

Internal Members: Marios Ioannidis
Professor, Dept. of Chemical Engineering, University of Waterloo
Michael Pope
Assistant Professor, Dept. of Chemical Engineering,
University of Waterloo

Author's Declaration

I hereby declare that I am the sole author of this thesis. This is a true copy of the thesis, including any required final revisions, as accepted by my examiners.

I understand that my thesis may be made electronically available to the public.

Abstract

Removal of sulphur from fossil fuels is important in order to avoid the emission of sulphur oxides into the atmosphere, exposure to which has negative health and environmental effects. Sulphur is removed from refinery petrochemical products via the Claus process which contains a waste heat boiler (WHB). These WHBs are exposed to extreme temperatures and corrosive conditions, yet they are expected to operate continuously for years at a time.

Typically WHBs have been designed using empirical correlations and heuristics, but more recently using process and multiphysics simulation. In this work a proof of concept for the numerical simulation of a WHB and its protective insulation is demonstrated. Continuum multiphysics models for both shell and tube side of a WHB are developed. An iterative coupling method for the determination of steady-state numerical solution of these models is then used to simulate a sub-region of a typical WHB.

Simulation results for the tube-side of the WHB predict both the temperature profile and nature of the turbulent energy transport in the inlet region, highlighting complex flow profiles. Simulations of the shell-side of the WHB predict the multiphase convective boiling behaviour in the bulk (far from wall effects). Finally, preliminary results of the coupled shell/tube configurations are presented and compared to previous results.

Acknowledgements

I would like to extend my heartfelt gratitude to my family for all the encouragement and support that helped make this possible.

Thank you Pamela for braving this journey with me.

Table of Contents

xii

List of Tables

List of Figures

Chapter 1

Introduction

1.1 Waste Heat Boilers and Challenges

Exposure to sulphur oxides in air can harm the human respiratory system impeding breathing, particularly in young, elderly, and those with asthma. Sulphur oxides also contribute to particulate matter, which can be entrained into the lungs. The effects of sulphur oxide contamination at higher concentrations include: vegetation damage, acid rain, and other negative effects on the environment. Hence from 1985 to 2006, through strict government enforcement, the rate of sulphur oxides emissions in Canada has decreased by 47% [1].

Under the Environmental Protection Act of 1999 the government of Canada regulates air quality, including sulphur oxide emissions. Most sulphur oxides enter the atmosphere through the burning of fossil fuels, notably coal and derivatives of "sour" (high in sulphur content) crude oil. Therefore much of the petrochemical industry must "sweeten" (lower the sulphur content) its crude before sending it to market. The sulphur extracted is then used in many applications such as the vulcanization of rubber, as a pesticide, and in the production of sulphuric acid. At a petrochemical refinery the sulphur recovery unit (SRU) plays a critical role in limiting the sulphur emissions and recovering sulphur for later cost recovery.

Most SRUs in operation today are built around the Claus process [4], possibly with additional advanced sulphur recovery techniques to further reduce emissions. The Claus process starts off with a reaction furnace where a third of the input H_2S is burned into water and SO_2 at very high temperatures according to the following reaction:

$$2\,H_2S + 3\,O_2 \longrightarrow 2\,SO_2 + 2\,H_2O$$
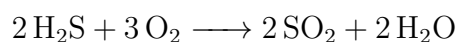
Figure 1.1: Sulphur removed from crude at Suncor operation, Fort McMurray. Alberta alone produced 3.9 million tons of sulphur in 2017 [2, 3].

The resulting flow is then cooled through the tubes of a shell and tube heat exchanger, with water and steam occupying the shell side. After this, the flow is passed through three stages of catalyst converters to combine the remaining H_2S and SO_2 into elemental sulphur and water. In between each catalytic converter is a condenser which removes the elemental sulphur from the flow via condensation followed by a re-heater.

$$4\,H_2S + 2\,SO_2 \longrightarrow 3\,S_2 + 4\,H_2O$$
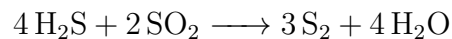
The reaction furnace typically reaches temperatures upwards of 1000 °C and is exposed to corrosive gases. Additionally, concentrations of hydrogen sulphide are at levels which pose significant safety hazards. Thus, the furnace is lined with insulating brick and mortar in order to shield the steel shell from the elevated temperatures and corrosive conditions.

The shell and tube heat exchanger, known as a waste heat boiler (WHB), is also exposed to these extreme conditions, particularly at the inlet before the process gases have sufficiently cooled. The front face of the WHB is generally protected by a ferrule system which is comprised of a ceramic ferrule extending several (tube) diameters into the tube, wrapped in a a highly insulating ceramic paper material. Typically these SRU units are expected to run continuously for years, only being brought down during plant turnovers
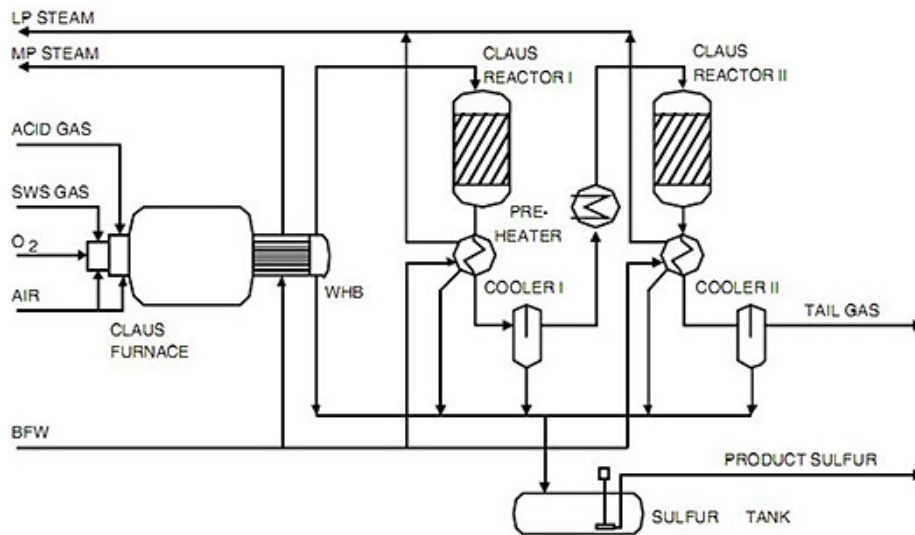
Figure 1.2: P&ID of the Claus Process used in most SRUs, sour gas and air are partially combusted in the reaction furnace, the output of which is cooled by the waste heat boiler. The process then flows through a number of catalytic converters to combine hydrogen sulphide and sulphur dioxide into water and elemental sulphur. Condensers remove the sulphur from the flow, before the process gas is reheated before the next converter as high temperatures thermodynamically favour the production of sulphur. [5].

every five years or so. Were the SRU shutdown prematurely, the whole refinery would have to cease operations in order to comply with regulations, which would be very costly. This means that the system must be extremely robust and that metal oxidization in the WHB should be kept to a minimum.

Within the WHB there are many phenomena occurring simultaneously including: phase change (shell-side boiling), turbulence (both shell and tube sides), and heat transfer. The process gas is cooled via heat transport through the walls from the tube side to the shell side, turbulent transport in the gas phase, and convective boiling in the liquid phase. There is phase change in the form of boiling on the shell side, where 40 *bar* steam is typically generated for use elsewhere in the plant. Flows, both in the tube and the shell, are turbulent due to high flow rates and the churning effect of bubbles in the boiling water.

1.2 Research Motivation and Industrial Application

Typically shell and tube heat exchangers have been designed using empirical correlations and heuristics, but more recently using process and multiphysics simulations. Simulation based design employs either lumped unit mass and energy balances or continuum multiphysics models. Lumped models use averaged heat transfer coefficients, such as the Sieder-Tate correlation [6], and log mean temperature differences between the shell and tube. While this may be sufficient for the overall sizing of a WHB, local effects are averaged-out, which creates issues when local phenomena might be a limiting factor or failure mode in actual operation. In a WHB it is quite possible that while the overall rate of heat transfer is low enough to avoid failure, certain regions may experience higher fluxes resulting in higher temperatures or departure from nucleate boiling.

Due to the local nature of these phenomena there is a demand for the investigation of these systems at a smaller scale when sizing and designing a WHB and its insulation. Yet because of the extreme conditions of the process, with its elevated temperatures and toxic products, it is very challenging to measure local process data. Therefore multiphysics simulations are a necessary approach to better understand system performance and design future systems.

A significant amount of SRU infrastructure is already in place and fossil fuel demands are forecast to rise. For example, US crude production is expected to increase from 12 million barrels per day today to 14 by 2027 according to the U.S. Department of Energy [7]. This trend has and will continue to put pressure on current capacity, demanding more of SRUs and their waste heat boilers. A better understanding of their capacity limits is valuable in avoiding costly shutdowns and capital projects.

1.3 Research Objectives

The overall objective of this research project is to formulate models for both shell and tube side of a WHB and develop an iterative coupling method to demonstrate a proof of concept for a coupled approach to modelling a WHB. Specific objectives include:

- Selection of appropriate models governing flow, phase change, and heat transfer in both the shell and tube side of a WHB

- Use of iterative coupling to determine steady-state coupled flow and temperature profiles in a sub-domain of the boiler

- Present a proof of concept series of simulations with convergence demonstrating the localized modelling of a WHB

1.4 Thesis Organization

This thesis is organized into six chapters: Chapter 1 - Introduction, Chapter 2 - Background and Literature Review, Chapter 3 - Tube Side Model and Simulations, Chapter 4 - Shell Side Model and Simulations, Chapter 5 - Coupled Model and Simulations, Chapter 6 Conclusions and Future Work.

Chapter 2 describes the relevant knowledge needed to approach this work. A detailed description of the physical system is presented along with an overview of the phenomena present. Following, the effects of and theory behind turbulence coupled with heat transfer are discussed. Next the multiphase model used for shell-side simulations is presented along with a mechanistic model for nucleate boiling. Finally previous works coupling two domains are discussed and the numerics needed to solve the system numerically are presented.

Chapter 3 presents the set-up and results for the tube side portion of the simulations performed. Numerical methods used, along with boundary conditions and assumptions are put forward. Following, the results are presented and their validity discussed along with the impact of key phenomena.

Chapter 4 follows a similar format to chapter 3 now pertaining to the shell side simulations. Furthermore, key simulation parameters are identified.

Chapter 5 contains the results of the coupling of both shell and tube side simulations. Along with coupling convergence, the impact of coupling is compared to the results from chapters 3 and 4.

Lastly, chapter 6 summarizes the conclusions derived from this work and makes recommendations on how it may be continued.

Chapter 2

Background and Literature Review

This section will summarize the necessary background knowledge to formulate a model for the simulation of the shell and tube sides of a waste heat boiler (WHB). First, a brief background of WHBs will be presented along with the equations governing single phase fluid flow. Subsequently, the impact of turbulence on fluid flow and heat transfer will be discussed along with numerical methods of representing turbulence. Following this, the modelling of two phase flow will be outlined along with the two fluid model. The phenomena of boiling, and how to represent it within an Euler-Euler multiphase fluid model will be presented. Finally, previous work in coupling similar systems will be reviewed followed by a brief overview of the numerics involved.

2.1 Waste Heat Boiler Detailed Background

Waste heat boilers are shell and tube heat exchangers in which a hot process fluid travels through the tubes, and through thermal conduction through the tubes, produces high pressure steam in the shell. The tube side process gas is produced by a reaction furnace at temperatures over 1000 °C. At these temperatures and with exposure to hydrogen sulphide gas, corrosion of the WHB and reaction furnace occurs at an unacceptably high rate. In order to prevent this corrosion a refractory lining is placed along the inner surfaces of the reactor and along the front tube sheet of the WHB as seen in Fig. 2.1.

The gaseous phase entering the tube side of the WHB boiler is at a much higher temperature than the boiling water of the shell side. This gradient in temperature results in heat flux through the metal tubes cooling the process gas and vaporizing the liquid

7
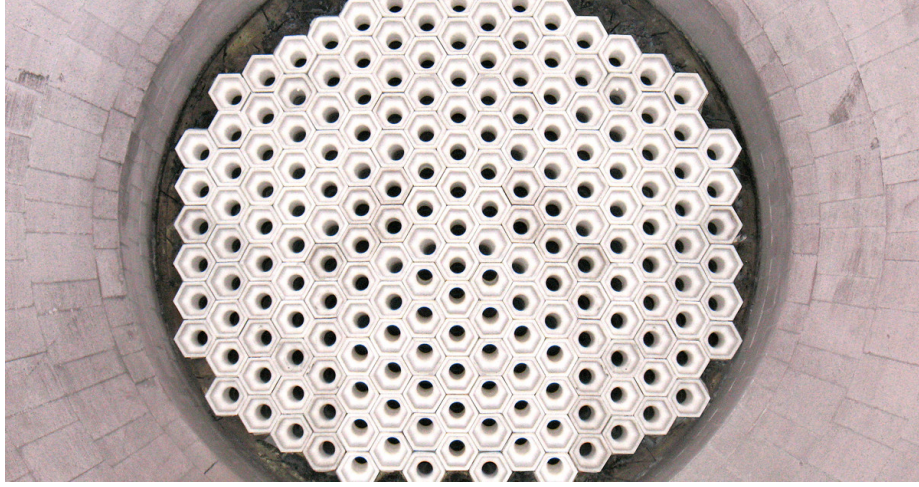
Figure 2.1: The WHB tubesheet facing the reaction furnace with installed ferrule thermal protection in a hexagonal pattern [8].

water. The insulating ceramic ferrule works by introducing a layer of material with high thermal resistance in-between the process gas and the metal of the tubesheet keeping the inlet of the WHB cool and corrosion free.

The process gas flow enters the ferrules at approximately 80 m/s, which corresponds to a Mach number of $\approx$ 0.1, and may therefore be approximated as an incompressible flow [9]. Due to the large changes in temperature and pressure present in the system, variation in fluid density is expected, but for the purpose of this work incompressible flow is suitable for proof of concept. The Navier-Stokes equations for an incompressible fluid govern the dynamics of fluid flow, comprised of three coupled conservation equations: mass, momentum, and energy. The conservation of mass, or continuity equation, is:

$$\nabla \cdot \boldsymbol{V} = 0 \tag{2.1}$$

where $\boldsymbol{V}$ is the velocity vector of the fluid.

The conservation of momentum equation may be viewed as the application of Newton's second law to a (fluid) continuum. It is a balance of the forces acting upon an infinitesimal volume of fluid, altering its motion, and takes the form of Eqn. (2.2) for an incompressible Newtonian fluid [10].

$$\rho \left(\frac{\partial \boldsymbol{V}}{\partial t} + \boldsymbol{V} \cdot \nabla \boldsymbol{V} \right) = -\nabla p + \mu \left(\nabla^2 \boldsymbol{V} \right) \tag{2.2}$$

where ρ and p are the density and the fluid pressure respectively while for a Newtonian fluid:

$$\boldsymbol{\tau} = \mu\dot{\gamma} \tag{2.3}$$

where $\boldsymbol{\tau}, \mu, \dot{\gamma}$ are the sheer stress, absolute viscosity, and rate of deformation respectively. The conservation of energy equation takes the following form:

$$
\begin{aligned}
\rho C_v \left(\frac{\partial T}{\partial t} + \boldsymbol{V} \cdot \nabla T \right) = k\nabla^2 T + 2\mu &\left[\left(\frac{\delta \boldsymbol{V}_x}{\delta x} \right)^2 + \left(\frac{\delta \boldsymbol{V}_y}{\delta y} \right)^2 + \left(\frac{\delta \boldsymbol{V}_z}{\delta z} \right)^2 \right] \\
+ \mu &\left[\left(\frac{\delta \boldsymbol{V}_x}{\delta y} + \frac{\delta \boldsymbol{V}_y}{\delta x} \right)^2 + \left(\frac{\delta \boldsymbol{V}_x}{\delta z} + \frac{\delta \boldsymbol{V}_z}{\delta x} \right)^2 + \left(\frac{\delta \boldsymbol{V}_y}{\delta z} + \frac{\delta \boldsymbol{V}_z}{\delta y} \right)^2 \right]
\end{aligned}
\tag{2.4}
$$

where T is the temperature, k the thermal conductivity and C_v the specific heat at constant volume.

In cases where flow is travelling at a slower velocity (less than a third the speed of sound) the viscous heating terms may be neglected as shown in a brief scaling analysis in appendix 2.

$$\rho C_v \left(\frac{\partial T}{\partial t} + \boldsymbol{V} \cdot \nabla T \right) = k\nabla^2 T \tag{2.5}$$

Energy is also conducted through the solid medium, in this case the conservation of energy equation simplifies to Eqn. (2.6),

$$\frac{\partial T}{\partial t} = \frac{k}{\rho C_p} \nabla^2 T \tag{2.6}$$

The conservation of mass, momentum, and energy equations presented describe all fluid flows for an incompressible Newtonian fluid, yet due to the limits of current computational resources in order to feasibly approach the process conditions within a WHB these equations must be altered as resolving these equations at the time and length scales needed for these conditions is prohibitively expensive.

First, for turbulence a method of coarsening out the velocity fluctuations and stabilizing the simulation will be needed, and secondly in the shell side a method for handling two fluid flow without resolving each interface and flow around and within bubbles is required. For these two challenges standard resolutions will be presented in Section 2.2 and Section 2.3 respectively.

9

2.2 Turbulence (RANS) and Coupling with Heat Transfer

Under typical process conditions, the volumetric flow rate and peak velocities are relatively high through the inlet of the ferrule and tube, approaching $80\ m/s$ in some cases. Given typical tube diameters of $25\ cm$, the corresponding Reynolds number is very large under these conditions, $Re > 100,000$, resulting in highly turbulent flow:

$$Re = \frac{V\,D}{\nu} \tag{2.7}$$

where D is pipe diameter and ν is the kinematic viscosity of the fluid. The Reynolds number is the ratio of inertial forces to viscous forces and values at this magnitude imply that inertial forces are highly dominant, leading to turbulent flow [9].

Turbulence arises in fluid flow when inertial forces exceed the capacity of viscous sheer stresses to stabilize the flow and local fluctuations in velocity are not dampened. It is characterized by a highly chaotic flow profile, with no local steady state, in which turbulent eddies break down into smaller and smaller length scales following the energy cascade eventually dissipating into heat. This turbulence arises due to minute vibrations and instabilities which are not sufficiently dampened and propagate throughout the medium [11].

Turbulent eddies that form from velocity fluctuations result in advective transport, yet the scale of this advection is so small and chaotic that it is typically approximated as a turbulent "diffusive" flux. Due to the chaotic nature of turbulence, capturing this phenomena in a numerical simulation is quite challenging. Multiple approaches for capturing the effects of turbulence have been proposed within the realm of Computational Fluid Dynamics (CFD) which can be divided into three separate classes: Reynolds Averaged Navier Stokes (RANS), Large Eddie Simulations (LES), and Direct Numerical Simulation (DNS).

The Navier Stokes equations are thought to adequately model fluid flow, including turbulence. However, turbulence occurs at such a small spacial and temporal scale that to solve it directly is very expensive computationally and only feasible for very small domains. At its smallest scale, the Kolmogorov length scale, turbulence is dissipated into heat through viscous action [13]. In order to fully resolve turbulence with just the Navier Stokes equations, these length scales need to be captured.

$$\eta = \left(\frac{\nu^3}{\epsilon}\right)^{1/4} \tag{2.8}$$

10
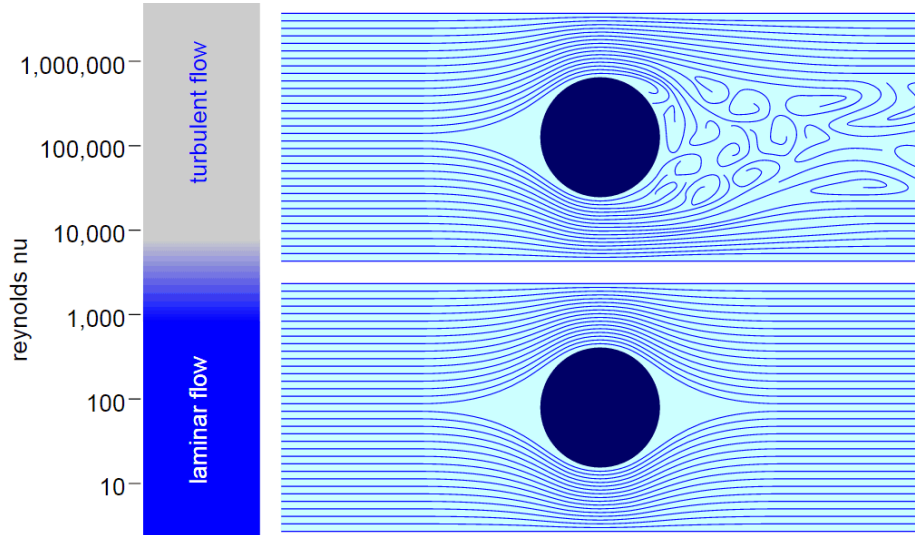
Figure 2.2: A comparison of orderly laminar flow below, notice the smooth streamlines, and chaotic turbulent flow above where multiple eddies form after the sphere [12].

$$t_\eta = \left(\frac{\nu}{\epsilon}\right)^{1/2} \tag{2.9}$$

where ϵ is the rate of turbulent energy dissipation per unit mass. Equation (2.8) and Eqn. (2.9) provide the length and time scale of these Kolmogorov eddies respectively.

In a typical WHB tube with an average flow of $50\ m/s$ and a kinematic viscosity of $1.5 \times 10^{-4}\ m^2/s$ using a mixing length model with moderately turbulent conditions the approximate turbulent scales are $200\ \mu m$ and $3 \times 10^{-4}\ s$ for length and time respectively. In order to resolve these eddies the mesh and time-steps would have to capture these values, when this is done it is known as DNS [14]. DNS has niche applications such as in simulating high fidelity reference cases, particularly in systems where experimental results would be hard to obtain, for comparison to other industrial scale turbulence models. Due to its exceptional computational costs DNS has not seen penetration into the wider CFD market and remains primarily a research tool.

Turbulent dissipation through the formation and "cascade" of eddies ranges from scales on the order of the geometric length scale (pipe diameter for instance) down to the Kolmogorov length scale. Most of the momentum in turbulent flow, and hence most of the kinetic energy, is contained within the larger eddies along this spectrum. Furthermore, larger eddies are dependent on flow geometry, for example being generated by a backward facing step, on the other hand the smallest eddies are independent of geometry and behave

isotropicaly. It is from these observations that the LES models were developed [15].

LES models function by resolving the larger turbulent eddies while coarsening out the smaller eddies through some sub-model. Since the smallest eddies are mostly independent of flow geometry and are isotropic, it may be argued that coarsening out their effect should have negligible effects on the overall pattern of flow. A natural question that arises when performing an LES simulation is: at what length scale should the eddies be coarsened out? Typically this is done in an *ad hoc* way using the mesh spacing of the simulation, any eddy smaller than two mesh spacings will not be able to be resolved and is therefore coarsened out. Therefore, there is an inherent trade off between mesh density and turbulence accuracy in LES simulations, as the mesh scale decreases a LES run will approach the accuracy of a DNS but the computational resources required also increase in part.

The most widely used method for tackling turbulence in CFD is RANS. RANS models use time averaging to smooth out the turbulence and resolve the mean flow of fluid by adjusting the viscosity based off of conserved turbulent properties. This adjusted viscosity also has the effect of stabilizing the computation where as pure turbulence typically will lead to an unstable solve unless the length and time scales resolved are small enough.

Consider that the flow properties of velocity and pressure can be described as a mean value plus some variation around this mean.

$$\boldsymbol{V}_i = \bar{\boldsymbol{V}}_i + \boldsymbol{V}_i' \tag{2.10}$$

$$p = \bar{p} + p' \tag{2.11}$$

where the superscript $'$ denotes a fluctuation and $^-$ denotes a time averaged value such that:

$$\bar{\theta} = \frac{1}{2T} \int_{-T}^{T} \theta dt \tag{2.12}$$

When the time interval of averaging is selected to be large enough such that the turbulent fluctuations are filtered out, but small enough that bulk flow changes are unaffected, by definition:

$$\bar{\boldsymbol{V}}' = \bar{p}' = 0 \tag{2.13}$$

by averaging $\boldsymbol{V}_i$, p and combining Eqn. (2.10), Eqn. (2.11) and Eqn. (2.13):

$$\bar{\boldsymbol{V}}_i = \bar{\bar{\boldsymbol{V}}}_i + \bar{\boldsymbol{V}}' = \bar{\bar{\boldsymbol{V}}}_i \tag{2.14}$$

similarly

$$\bar{p} = \bar{\bar{p}} \tag{2.15}$$

First applying the averaging to Eqn. (2.1):

$$\overline{\nabla \cdot \boldsymbol{V}} = \nabla \cdot \bar{\boldsymbol{V}} = 0 \tag{2.16}$$

Equation (2.2) may also be rewritten in the conservation form, where the momentum equation takes the form of:

$$\rho \left(\frac{\partial \boldsymbol{V}_i}{\partial t} + \nabla \cdot (\boldsymbol{V}_i \boldsymbol{V}) \right) = -\frac{\partial p}{\partial x_i} + \mu \left(\nabla^2 \boldsymbol{V}_i \right) \tag{2.17}$$

where the subscript i denotes the direction specified by a basis vector.

Inserting Eqn. (2.10) and Eqn. (2.11) into and then applying the time averaging to Eqn. (2.17):

$$\overline{\rho \left(\frac{\partial \left(\bar{\boldsymbol{V}}_i + \boldsymbol{V}_i' \right)}{\partial t} + \nabla \cdot \left(\left(\bar{\boldsymbol{V}}_i + \boldsymbol{V}_i' \right) \left(\bar{\boldsymbol{V}} + \boldsymbol{V}' \right) \right) \right)} = -\overline{\frac{\partial \left(\bar{p} + p' \right)}{\partial x_i}} + \overline{\mu \left(\nabla^2 \left(\bar{\boldsymbol{V}}_i + \boldsymbol{V}_i' \right) \right)} \tag{2.18}$$

with some rearrangement:

$$\rho \left(\frac{\partial \left(\bar{\bar{\boldsymbol{V}}}_i + \bar{\boldsymbol{V}'}_i \right)}{\partial t} + \nabla \cdot \left(\overline{\left(\bar{\boldsymbol{V}}_i + \boldsymbol{V}_i' \right) \left(\bar{\boldsymbol{V}} + \boldsymbol{V}' \right)} \right) \right) = -\frac{\partial \left(\bar{\bar{p}} + \bar{p}' \right)}{\partial x_i} + \mu \left(\nabla^2 \left(\bar{\bar{\boldsymbol{V}}}_i + \bar{\boldsymbol{V}'}_i \right) \right) \tag{2.19}$$

further simplification yields:

$$\rho \left(\frac{\partial \bar{\boldsymbol{V}}_i}{\partial t} + \nabla \cdot \left(\sum_{j=1}^{3} \bar{\boldsymbol{V}}_i \bar{\boldsymbol{V}}_j \boldsymbol{e}_j + \sum_{j=1}^{3} \overline{\boldsymbol{V}_i' \boldsymbol{V}_j'} \boldsymbol{e}_j \right) \right) = -\frac{\partial \bar{p}}{\partial x_i} + \mu \left(\nabla^2 \bar{\boldsymbol{V}}_i \right) \tag{2.20}$$

where $\boldsymbol{e}_j$ are the basis vectors. Finally:

$$\rho \left(\frac{\partial \bar{\boldsymbol{V}}_i}{\partial t} + \nabla \cdot \left(\bar{\boldsymbol{V}}_i \bar{\boldsymbol{V}} \right) \right) = -\frac{\partial \bar{p}}{\partial x_i} + \mu \left(\nabla^2 \bar{\boldsymbol{V}}_i \right) - \rho \nabla \cdot \left(\sum_{j=1}^{3} \overline{\boldsymbol{V}_i' \boldsymbol{V}_j'} \boldsymbol{e}_j \right) \tag{2.21}$$

typically rewritten as:

$$\rho \left(\frac{\partial \bar{\boldsymbol{V}}_i}{\partial t} + \nabla \cdot \left(\bar{\boldsymbol{V}}_i \bar{\boldsymbol{V}} \right) \right) = -\frac{\partial \bar{p}}{\partial x_i} + \nabla \cdot \left(\mu \nabla \bar{\boldsymbol{V}}_i - \rho \sum_{j=1}^{3} \overline{\boldsymbol{V}_i' \boldsymbol{V}_j'} \boldsymbol{e}_j \right) \tag{2.22}$$

Equation (2.22) closely resembles the standard conservative form of the Navier Stokes equations for momentum conservation, with an additional term on the right hand side. The

13

conserved variable is now the time averaged momentum as opposed to the instantaneous momentum and the additional term accounts for the impact of turbulent fluctuations. While the time averaged value of fluctuations is zero, the product of two fluctuations when time averaged is not zero, hence the additional term which serves as a measure of turbulent energy.

This remaining term creates what is known as the "closure problem", in order to model turbulence using only mean flow parameters the fluctuating term must be modelled as some function of mean flow values. In two-equation models, the most commonly used RANS closures, the Boussinesq approximation is used to solve the closure problem. Boussinesq proposed that the Reynolds stresses acted similarly to viscosity such that [16]:

$$-\rho \sum_{j=1}^{3} \overline{V_i' V_j'} \boldsymbol{e}_j = \mu_t \nabla \bar{V}_i + \rho \sum_{j=1}^{3} \frac{2\boldsymbol{k}_i}{3} \delta_{ij} \boldsymbol{e}_j \tag{2.23}$$

where μ_t is the turbulent viscosity and $\boldsymbol{k}$ is defined as:

$$\boldsymbol{k}_i = \frac{1}{2} \overline{V_i' V_i'} \tag{2.24}$$

Two equation models assume that the turbulent stresses, and by extension μ_t and $\boldsymbol{k}$, are isotropic such that the turbulent kinetic energy is:

$$k = \frac{1}{2} \sqrt{\sum_{i=1}^{3} \overline{V_i' V_i'}} \tag{2.25}$$

Equation (2.23) and Eqn. (2.22), returning to the convective form, yield the following:

$$\rho \left(\frac{\partial \bar{V}}{\partial t} + \bar{V} \cdot \nabla \bar{V} \right) = -\nabla \bar{p}^* + (\mu + \mu_t) \nabla^2 \bar{V} \tag{2.26}$$

where $\bar{p}^* = \bar{p} + \frac{2k}{3}$ represents the modified turbulent pressure.

Similarly to the momentum equations, the energy equation takes the form of an increased thermal diffusion.

$$\rho C_v \left(\frac{\partial \bar{T}}{\partial t} + \bar{V} \cdot \nabla \bar{T} \right) = (k + k_t) \nabla^2 \bar{T} \tag{2.27}$$

where k_T is the turbulent thermal conductivity.

$$k_t = \frac{C_p \, \mu_t}{Pr_t} \tag{2.28}$$

14

where Pr_t is the turbulent Prandtl number, typically given as 0.85 for most fluids but may range from 0.7 to 0.9 according to [17].

The six unknown turbulent Reynolds stresses that formed the closure problem have now been reduced to two unknowns, μ_t and k. Two equation models also introduce another variable which is a measure of the dissipation of turbulent kinetic energy. Both k and this dissipation are conserved variables for which a PDE is formulated and solved within the numerical method of choice, hence they are two equation models. The turbulent variables are then linked to turbulent viscosity via some algebraic equation such that $\mu_t = f(k, \omega)$. In the previous equation the variable used to track turbulent dissipation is the specific turbulence dissipation rate which is the rate at which turbulent kinetic energy is lost per unit of turbulent kinetic energy.

There are many different two equation models, each with their own strengths and weaknesses. The two most widely used turbulence models are the $k - \epsilon$ and $k - \omega$ models. The $k - \epsilon$ being very robust and well suited to high Reynolds number flows, while the $k - \omega$ model is most accurate for low Reynolds number flows [18]. The $k - \omega$ model accomplishes this by solving for the turbulence variables all the down to the viscous sub-layer adjacent to the wall, in this layer flow is actually laminar due to the zero velocity at the wall itself. On the other hand $k - \epsilon$ uses additional closures near solid boundaries, or "wall" functions, and assumes that the nearest node to the wall falls within the logarithmic layer where velocity increases logarithmically as a function of distance from the wall. By solving turbulence and flow much closer to the wall, $k - \omega$ performs better when resolving phenomena that occur between the wall and the fluid, namely heat transfer.

The $k - \omega$ SST model is a blending of these two models, combining the robustness of $k - \epsilon$ and the near wall performance of $k - \omega$. Proposed by Menter, the model solves the following two equations for the turbulent variables, the overbars indicating averaging has been dropped for ease of reading [19]:

$$\frac{\partial (\rho k)}{\partial t} + \frac{\partial (\rho \boldsymbol{V}_j k)}{\partial x_j} = P - \beta^* \rho \omega k + \frac{\partial}{\partial x_j} \left((\mu + \sigma_k \mu_t) \frac{\partial k}{\partial x_j} \right) \tag{2.29}$$

$$\frac{\partial (\rho \omega)}{\partial t} + \frac{\partial (\rho \boldsymbol{V}_j \omega)}{\partial x_j} = \frac{\gamma \rho}{\mu_t} P - \beta \rho \omega^2 + \frac{\partial}{\partial x_j} \left((\mu + \sigma_\omega \mu_t) \frac{\partial \omega}{\partial x_j} \right) + 2 (1 - F_1) \frac{\rho \sigma_{\omega 2}}{\omega} \frac{\partial k}{\partial x_j} \frac{\partial \omega}{\partial x_j} \tag{2.30}$$

The turbulent viscosity is calculated in Eqn. (2.31):

$$\mu_t = \frac{\rho a_1 k}{max(a_1 \omega, \Omega F_2)} \tag{2.31}$$

15

where:

$$P = \boldsymbol{\tau}_{ij} \frac{\partial \boldsymbol{V}_i}{\partial x_j} \tag{2.32}$$

$$\boldsymbol{\tau}_{ij} = \mu_t \left(\frac{\partial \boldsymbol{V}_i}{\partial x_j} + \frac{\partial \boldsymbol{V}_j}{\partial x_i} \right) - \frac{2}{3} \rho k \delta_{ij} \tag{2.33}$$

where the constants σ_ω, σ_k, β, and γ have been blended using:

$$\phi = F_1 \phi_1 + (1 - F_1) \phi_2 \tag{2.34}$$

$$F_1 = \tanh \left(\left(\left(\min \left[\max \left(\frac{\sqrt{k}}{\beta^* \omega d}, \frac{500\mu}{d^2 \omega \rho} \right), \frac{4 \rho \sigma_{\omega 2} k}{CD_{k\omega} d^2} \right] \right)^4 \right) \right) \tag{2.35}$$

$$CD_{k\omega} = \max \left(2 \rho \sigma_{\omega 2} \frac{1}{\omega} \frac{\partial k}{\partial x_j} \frac{\partial \omega}{\partial x_j}, 10^{-20} \right) \tag{2.36}$$

$$F_2 = \tanh \left(\left[\max \left(2 \frac{\sqrt{k}}{\beta^* \omega d}, \frac{500\mu}{d^2 \omega \rho} \right) \right]^2 \right) \tag{2.37}$$

$$\Omega = \frac{1}{\sqrt{2}} \left(\frac{\partial \boldsymbol{V}_i}{\partial x_j} - \frac{\partial \boldsymbol{V}_j}{\partial x_i} \right) \tag{2.38}$$

$$\gamma_1 = \frac{\beta_1}{\beta^*} - \frac{\sigma_{\omega 1} \kappa^2}{\sqrt{\beta^*}} \tag{2.39}$$

$$\gamma_2 = \frac{\beta_2}{\beta^*} - \frac{\sigma_{\omega 2} \kappa^2}{\sqrt{\beta^*}} \tag{2.40}$$

Constant	Value
σ_{k1}	0.85
σ_{k2}	1.0
$\sigma_{\omega 1}$	0.5
$\sigma_{\omega 2}$	0.856
β_1	0.075
β_2	0.0828
β^*	0.09
κ	0.41
a_1	0.31

Table 2.1: k-ω SST Constants

16

2.3   Two-fluid Model

In the shell side of a WHB, there are three phases present: solid, gas, and liquid. The solid is stationary and easily approximated by no-slip boundary conditions and simulation domain geometry. The fluid domain, however, is multiphase with gas dispersed in liquid with significant mass, momentum, and energy transfer between the two. Capturing this WHB system requires a model which is capable of accounting for both liquid and gas phases, their interactions, and phase change (boiling).

Typically there are three approaches to the modelling of two fluid flows: Euler-Euler, volume of fluid (VOF), and the mixture model [20]. The VOF model works by tracking the interface between the two phases and requires a very high mesh density in the vicinity of the interface in order to properly capture the energy exchanges between each phase. Hence the computational effort to solve a VOF system scales with the interfacial area. In a WHB system, where bubbles nucleate on solid surfaces and disperse into the liquid bulk, the VOF method becomes prohibitively expensive. The mixture model approximates a multiphase fluid flow as a single mixture in which the volume fraction of the dispersed phase affects the mixture flow properties, such as viscosity and density. While less computationally expensive than VOF, it is less accurate and a poor fit for heterogeneous mixtures which renders it unsuitable for this work.

In the case of the two fluid or Euler-Euler model both the phases are considered as a continuous fluid with their own sets of conservation equations for mass, momentum, and energy [21]. These two equations are then coupled via a set of interphase transfer terms. In order to accomplish this, a time averaging is used to solve for the overall macroscopic flow as opposed to the instantaneous flow profile.

The mass conservation for a phase q in the two fluid model is as follows [21]:

$$\frac{\partial(\alpha_q\overline{\overline{\rho_q}})}{\partial t} + \nabla \cdot (\alpha_q\overline{\overline{\rho_q}}\widehat{\boldsymbol{v}}_q) = \Gamma_q \tag{2.41}$$

where α_q is the time averaged phase fraction of the q phase, $\overline{\overline{\rho_q}}$ is the time averaged density of phase q, $\widehat{\boldsymbol{v}}_q$ is the time averaged phase velocity, and Γ_q is the overall mass transfer into the qth phase.

For momentum conservation, the governing equation for the q phase is:

$$\alpha_q\overline{\overline{\rho_q}}\left(\frac{\partial\widehat{\boldsymbol{v}}_q}{\partial t} + \widehat{\boldsymbol{v}}_q \cdot \nabla\widehat{\boldsymbol{v}}_q\right) = -\alpha_q\nabla\overline{\overline{P_q}} + \nabla \cdot \left[\alpha_q\left(\overline{\overline{\boldsymbol{\tau}_q}} + \boldsymbol{\tau}_q^T\right)\right] + \alpha\overline{\overline{\rho_q}}\widehat{\boldsymbol{g}} + \left(\overline{\overline{P_{qi}}} - \overline{\overline{P_q}}\right)\nabla\alpha_q$$
$$+ \left(\widehat{\boldsymbol{v}_{qi}} - \widehat{\boldsymbol{v}}_q\right)\Gamma_q + \boldsymbol{M}_{qi} - \nabla\alpha_k \cdot \overline{\overline{\boldsymbol{\tau}_{qi}}} \tag{2.42}$$

where $\overline{\overline{\pmb{\tau}_q}}$ is the time averaged phasic viscous stress tensor, $\overline{\overline{\pmb{\tau}_q^T}}$ the phasic turbulent stresses tensor, $\widehat{\pmb{g}}$ is the time averaged mass weighted gravitational acceleration, $\overline{\overline{P_q}}$ the time averaged phasic pressure, $\pmb{M}_q$ the interphase momentum exchange term, and the subscript $_i$ denotes an interfacial variable.

The contribution of interfacial viscous stresses is small in most cases excluding segregated flow, therefore in the dispersed flow regime it may be assumed to be negligible. Furthermore, in dispersed flow the interfacial pressures may be assumed to be equal and the dispersed phase pressure approximated via the interfacial pressure, $\overline{\overline{P_{c,i}}} \approx \overline{\overline{P_{d,i}}} = P_{int} = \overline{\overline{P_d}}$ [21, 22]. Lumping the momentum exchange due to mass transfer into the momentum exchange between phases term leads to the following momentum conservation equations for the continuous and dispersed phases:

$$\alpha_c \overline{\overline{\rho_c}} \left(\frac{\partial \widehat{\pmb{v}_c}}{\partial t} + \widehat{\pmb{v}_c} \cdot \nabla \widehat{\pmb{v}_c} \right) = -\alpha_c \nabla \overline{\overline{P_c}} + \nabla \cdot \left(\alpha_c \overline{\overline{\pmb{\tau}_c}} \right) + \alpha_c \overline{\overline{\rho_c}} \widehat{\pmb{g}} + \pmb{M}_c$$
$$+ \left(\overline{\overline{P_{int}}} - \overline{\overline{P_c}} \right) \nabla \alpha_c \tag{2.43}$$

$$\alpha_d \overline{\overline{\rho_d}} \left(\frac{\partial \widehat{\pmb{v}_d}}{\partial t} + \widehat{\pmb{v}_d} \cdot \nabla \widehat{\pmb{v}_d} \right) = -\alpha_d \nabla \overline{\overline{P_{int}}} + \nabla \cdot \left(\alpha_d \overline{\overline{\pmb{\tau}_d}} \right) + \alpha_d \overline{\overline{\rho_d}} \widehat{\pmb{g}} + \pmb{M}_d \tag{2.44}$$

In order to close the above equations, the momentum transfer terms must be defined. Many different closures exist, this work will look at three, the drag force, the virtual mass force, and the phase change force. Overbars and hats will be dropped in the subsequent formulations in order to improve legibility.

$$\pmb{M}_c = \pmb{M}_{c,drag} + \pmb{M}_{c,virtual\ mass} + \pmb{M}_{c,phase\ change} \tag{2.45}$$

$$\pmb{M}_c = -\pmb{M}_d \tag{2.46}$$

The drag force term represents the cumulative effects of form and skin drag on the dispersed phase. Skin drag is a consequence of viscous stresses along the dispersed phase surface which arise due to a relative velocity between the dispersed and continuous phase, $\pmb{v}_r = \pmb{v}_d - \pmb{v}_c$. Form drag on the other hand occurs due to a pressure differential in the continuous phase across the volume of a dispersed bubble, as the leading edge of the bubble will generate a high pressure zone and leave a low pressure zone in its wake. For a dispersed spherical bubble the contribution of drag to the momentum transfer is given by Eqn. (2.47):

$$\pmb{M}_{c,drag} = \frac{3}{4} \rho_c \alpha_d \frac{C_d}{d_d} \|\pmb{v}_r\| \pmb{v}_r \tag{2.47}$$

18

where C_D and d_d are the drag force coefficient and the diameter of the bubble respectively.

The virtual mass contribution to the momentum exchange is due to the wake of a bubble as it moves with a relative velocity in relation to the continuous phase. As the bubble moves, it drags a body of continuous phase along with it in its wake, which has the perceived effect of adding extra mass to the bubble, hence the term virtual mass. This added mass manifests itself when there is some acceleration of the bubble in relation to the continuous phase as this added mass must be accelerated as well. The contribution of virtual mas is as follows:

$$\boldsymbol{M}_{c,virtual\ mass} = \alpha_d \rho_c C_{VM} \left(\frac{\partial \boldsymbol{v}_r}{\partial t} + \boldsymbol{v}_d \cdot \nabla \boldsymbol{v}_d - \boldsymbol{v}_c \cdot \nabla \boldsymbol{v}_c \right) \tag{2.48}$$

where C_{VM} is the drag force coefficient.

The phase change force is the force required to accelerate mass that changes from one phase to the other. Assuming that the interfacial velocity in the liquid phase is equal to that of the dispersed phase the momentum exchange term is given by Eqn. (2.49):

$$\boldsymbol{M}_{c,phase\ change} = \Gamma_c \boldsymbol{v}_r \tag{2.49}$$

Finally, the P_{int} is given by Eqn. (2.50):

$$P_{int} = P_c - C_P \rho_c \boldsymbol{v}_r \cdot \boldsymbol{v}_r \tag{2.50}$$

The full thermal energy equation for a two phase system is given by Eqn. (2.51):

$$\alpha_k \overline{\overline{\rho_k}} \left(\frac{\partial \widehat{h_k}}{\partial t} + \widehat{\boldsymbol{v}_k} \cdot \nabla \widehat{h_k} \right) = -\nabla \cdot \alpha_k \left(\overline{\overline{\boldsymbol{q}_k}} + \boldsymbol{q}_k^T \right) - \widehat{\boldsymbol{v}_k} \cdot \nabla \cdot \left(\alpha_k \boldsymbol{\tau}_k^T \right) + W_{ki}^T + \alpha_k \left(\frac{\partial \overline{\overline{p_k}}}{\partial t} + \widehat{\boldsymbol{v}_k} \cdot \nabla \overline{\overline{p_k}} \right)$$

$$+ \alpha_k \overline{\overline{\boldsymbol{\tau}_k}} : \nabla \widehat{\boldsymbol{v}_k} + \Gamma_k \left(\widehat{h_{ki}} - \widehat{h_k} \right) + a_i \overline{\overline{q''_{ki}}} + \left(\overline{\overline{p_k}} - \overline{\overline{p_{ki}}} \right) \left(\frac{\partial \overline{\overline{\alpha_k}}}{\partial t} + \widehat{\boldsymbol{v}_k} \cdot \nabla \overline{\overline{\alpha_k}} \right)$$

$$+ \boldsymbol{M}_{ik} \cdot \left(\widehat{\boldsymbol{v}_{ki}} - \widehat{\boldsymbol{v}_k} \right) - \nabla \alpha_k \cdot \overline{\overline{\boldsymbol{\tau}_{ki}}} \cdot \left(\widehat{\boldsymbol{v}_{ki}} - \widehat{\boldsymbol{v}_k} \right) \tag{2.51}$$

where $\overline{\overline{\boldsymbol{q}_k}}$, and $\boldsymbol{q}_k^T$, are the mean conduction and turbulent heat fluxes, $\overline{\overline{q''_{ki}}}$ is the average heat transfer per unit of interfacial area, $\widehat{h_k}$, and $\widehat{h_{ki}}$ are the weighted virtual mean enthalpies in the bulk phase and at the interface respectively and W_{ki}^T is the work due to fluctuations in drag forces.

Clearly Eqn. (2.51) is quite complex, fortunately if the heat transfer and phase changes dominate the thermal energy exchanges we may neglect the mechanical terms, simplifying the problem greatly.

$$\alpha_k \overline{\overline{\rho_k}} \left(\frac{\partial \widehat{h_k}}{\partial t} + \widehat{\boldsymbol{v}}_k \cdot \nabla \widehat{h_k} \right) = -\nabla \cdot \alpha_k \left(\overline{\overline{\boldsymbol{q}_k}} + \boldsymbol{q}_k^T \right) + \Gamma_k \left(\widehat{h_{ki}} - \widehat{h_k} \right) + a_i \overline{\overline{q_k''}} \tag{2.52}$$

For a single component mixture two phase system (liquid water and water vapour) if the heat of vaporization is large with respect to the energy associated to the temperature difference between the interface and bulk, Eqn. (2.52) may be reduced further:

$$\alpha_k \overline{\overline{\rho_k}} \left(\frac{\partial \widehat{h_k}}{\partial t} + \widehat{\boldsymbol{v}}_k \cdot \nabla \widehat{h_k} \right) = -\nabla \cdot \alpha_k \left(\overline{\overline{\boldsymbol{q}_k}} + \boldsymbol{q}_k^T \right) + \Gamma_k \Delta H_{vap} + a_i \overline{\overline{q_k''}} \tag{2.53}$$

where ΔH_{vap} is the heat of vaporization.

Using the thermal resistance approach to close $\overline{\overline{q_k''}}$ with the Ranz-Marshall model [23] the last term on the right hand side of the energy equation may be solved for the continuous and dispersed phase:

$$\overline{\overline{q_c''}} = \overline{\overline{q_d''}} = h \left(T_d - T_c \right) \tag{2.54}$$

$$h = \frac{\kappa_c Nu_d}{d_d} \tag{2.55}$$

where κ_c is the thermal conductivity of the continuous phase.

$$Nu_d = 2.0 + 0.6 Re_d^{\frac{1}{2}} Pr^{\frac{1}{3}} \tag{2.56}$$

$$Re_d = \frac{\overline{\overline{\rho_c}} \widehat{\boldsymbol{v}}_r d_d}{\mu_c} \tag{2.57}$$

$$Pr = \frac{Cp_c \mu_c}{\kappa_c} \tag{2.58}$$

yielding the final form of the energy equation:

$$\alpha_k \overline{\overline{\rho_k}} \left(\frac{\partial \widehat{h_k}}{\partial t} + \widehat{\boldsymbol{v}}_k \cdot \nabla \widehat{h_k} \right) = -\nabla \cdot \alpha_k \left(\overline{\overline{\boldsymbol{q}_k}} + \boldsymbol{q}_k^T \right) + \Gamma_k \Delta H_{vap} + a_i h \left(T_d - T_c \right) \tag{2.59}$$

2.4 Boiling

Within the shell side of a WHB the primary heat sink for the tube side process gas is boiler feed water. This feed water is boiled along the surface of the tubes and in the process cools the process gas, also producing high pressure steam which may be used elsewhere in the plant for thermal duty. Boiling occurs when the partial pressure of the gaseous phase in equilibrium with the fluid exceeds the bulk pressure in the system. At this point mass from the liquid phase is converted to vapour which requires significant amounts of energy. The energy required to convert a unit of liquid to gas at a given temperature and pressure is referred to as the heat of vaporization, and it is this change which makes boiling liquid a particularly effective cooling mechanism when compared to simple convective or conductive heat transfer. Acting as an additional energy sink, the heat of vaporization requires energy without raising temperature and therefore maintaining a higher thermal gradient through the solid surface which drives further heat transfer.

When boiling a liquid on a surface, multiple mechanisms are possible depending on the degree of superheat (temperature above the boiling point) of the surface [24]. As fluid is heated above its boiling point, at low degrees of super heat it experiences natural convection boiling. At this point heat flux increases with the degree of superheat and no bubbles yet appear on the heating surface, instead convection currents dominate flow and vapour generation increases at the free surface of the fluid. When the degree of superheat increases further still bubbles begin to appear on the surface at nucleation sites and detach, rising through the liquid. This is process known as nucleate boiling during which heat flux increases rapidly with superheat, the churning effect on the liquid caused by departing bubbles serves to enhance heat transfer by disrupting thermal layers. For most applications this is the most desirable boiling regime as it provides the most heat transfer at reasonable degrees of super heat.

If the superheat continues to increase, boiling becomes so vigorous that the gaseous phase covers an ever larger portion of the surface area for boiling. Because gas tends to be a poor heat conductor compared to liquid, the gas begins to insulate the surface and actually reduces the rate of heat transfer until the Leidenfrost point is reached. This rapid decay in heat transfer is known as the transition region between nucleate and film boiling. After the Leidenfrost point is reached the surface is completely insulated by a vapour film and the heat flux is greatly reduced. Past this point radiation takes a more prominent role in heat transfer.

WHBs are designed to operate in the nucleate boiling range, as with most industrial boiling processes, and much effort has been made to better understand this region and delay
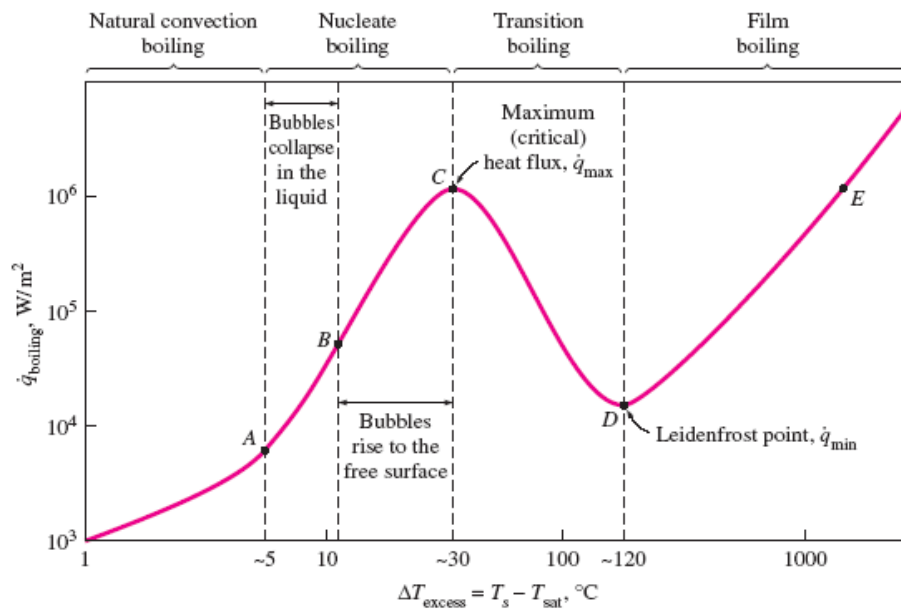
Figure 2.3: The heat flux as a degree of super heat for a boiling water system at one atmosphere, notice the great variations between the different boiling regimes [25].

the onset of film boiling [26]. There are two possible mechanisms for bubble nucleation, either homogeneous nucleation or heterogeneous nucleation. Homogeneous nucleation is the spontaneous formation of a bubble without some pre-existing gas pocket, and occurs either within the bulk liquid phase or along some smooth surface or particle. Heterogeneous nucleation on the other hand is the formation of a bubble at some pre-existing gas cavity either on some particle or in a defect on the boiling surface [27].

The pressure of a bubble within a liquid is given as a function of the meniscus radius of curvature:

$$\Delta P = \frac{2\gamma}{R'} \tag{2.60}$$

where ΔP is the pressure difference from the liquid to gas, γ is the interfacial tension, and R' is the meniscus radius of curvature.

When boiling, mass will leave the liquid phase to the vapour phase of a bubble so long as the pressure within the bubble is less than that in equilibrium with the liquid phase. As such it is clear from Eqn. (2.60) that as bubble radius decreases, vaporization (and hence bubble growth) becomes increasingly difficult due to the higher bubble pressure. This has the effect of making homogeneous boiling require very high degrees of superheat and unless precautions are taken heterogeneous boiling will occur long before homogeneous. Therefore real world engineering applications concern themselves with heterogeneous boiling.

As a bubble continues to grow, the radius generally increases facilitating further mass transfer by reducing the pressure inside the bubble and increasing the interfacial area. While the bubble grows and displaces liquid, a drag force is generated which helps keep the bubble attached to the surface. Subsequently as the gas-liquid interface slows an inertial force is generated on the bubble which helps lift it from the surface. Once surface tension and drag forces are overcome by buoyancy, inertial, and pressure forces the bubble departs the surface [27].

At this point the bubble disrupts the thermal boundary layer adjacent to the heated surface, bringing in cooler fluid from further afield which must be heated before another bubble forms leading to a wait time between bubbles [28]. The heating of this cooler fluid is one of the mechanisms responsible for the increased effective heat transfer of a boiling surface compared to convection and conduction. Vaporization of liquid and the energy this requires is another mechanism for enhanced cooling, multiple models of boiling have been formulated placing different emphasis on these mechanisms [26]. Earlier models such as those presented by Forster and Grief, or Han and Griffith assumed that the energy associated with phase change was negligible compared to the enhanced heat transfer caused by bubble churning [29, 28]. Mikic and Rohsenow postulated that an individual bubble

pulled a region of liquid around it with a radius equal to twice the departure diameter of the bubble and replaced it with cooler bulk liquid [30].

Later based off the assumption that liquid water is the wetting phase, Cooper and Lloyd proposed that as a bubble grows and leaves the footprint of its nucleation site it traps a thin micro-layer of liquid underneath it which rapidly vaporizes and cools the surface. Stephan and Hammer theorized that the three phase contact line where liquid, solid, and gas meet was the driver of heat exchange as liquid is readily heated and vaporized at this point [31, 32]. Kim found that the agitation and convection caused by bubble growth and departure were the biggest contributors to heat transfer but that phase change on the surface may contribute up to a quarter of energy exchange between the surface and fluids [26]. As it is clear there is little consensus on the impact of different heat transfer mechanisms present in boiling.

Part of the challenge is describing boiling is the highly non-linear nature of the phenomena. Shoji raises this concern in his work [33]. Within most boiling models nucleation sites are assumed to generate steam at a constant rate once activated, yet this simplification fails to account for nucleation site interactions. Furthermore, active nucleation sites do not strictly increase with higher super heats due to these interactions [34]. Shoji recommends that for better understanding of boiling, better models with higher resolutions capable of capturing nucleation site interactions and local variations in wall super heats are needed. Yet for engineering applications, such high fidelity simulations would be far too expensive computationally and therefore mechanistic models are standard practice.

2.5   Boiling and Modelling with Euler-Euler

Modelling boiling within an Euler-Euler multiphase model is a challenge, and has been explored within the field of nuclear engineering with a particular interest for stagnant vertical pool boiling. Part of this challenge arises from the Euler-Euler approach of averaging out the interfaces between the two phases, this is necessary to make the problem tractable from a computational standpoint due to the large amount of interfacial surface area generated during boiling which would be too prohibitive to track with a VOF approach. Yet boiling, being mass transfer between the two phases, is intrinsically an interfacial phenomenon. Therefore an approach which infers interfacial area, via other flow parameters known in Euler-Euler is needed.

Typically a heat balance is used to approximate the physics of nucleate boiling in Euler-Euler models. This is known as heat flux splitting where the heat flux through the solid

surface is split into three separate fluxes: quenching, bubble formation, and convective. Each heat flux is then evaluated via a mix of first principles and empirical closures [35].

$$q_w = q_{l\phi} + q_Q + q_e \tag{2.61}$$

In order to split the heat flux, first the area of the boiling surface is split into two: the portion of the area in which heat transfer is unaffected by the nucleation and departure of bubbles, and the portion of area that is. As the bubble grows, displacing liquid, and departs allowing liquid to return it enhances heat transfer in its near vicinity and as this portion of the overall surface grows so will the overall heat transfer.

$$1 = A_{l\phi} + A_Q \tag{2.62}$$

where A_Q is the fraction of the total surface area where heat transfer is directly influenced by the presence of departing bubbles and $A_{l\phi}$ is the portion of surface area undergoing convective heat transfer.

$$A_Q = min \left(\pi d_{dep}^2 N_{sd} , \, 1 \right) \tag{2.63}$$

here, d_{dep} is the diameter of departing bubbles from the surface and N_{sd} is the number of nucleation sites per unit area.

In the region outside the influence of departing bubbles, heat transport is governed via a heat transfer coefficient for standard single phase flows, assuming the wetting phase is the liquid:

$$q_{l\phi} = A_{l\phi} h_{l\phi} \left(T_W - T_\delta \right) \tag{2.64}$$

where $h_{l\phi}$ is resolved using a Reynolds analogy for heat fluxes depending on what turbulence model is used, and the subscript δ refers to the value at the nearest cell centre to the wall.

This region is treated as if boiling were not occurring and accounts for the standard convective heat transfer present in the system. It is weighted by the fractional area of boiling, and as such will reduce as boiling intensifies. While the heat transfer coefficient is not directly a function of boiling parameters, boiling increases the velocity of flow near the surface as liquid is displaced by gas and visa-versa, which increases the heat transfer coefficient.

The quenching heat flux is an enhanced heat flux which results from the departure of bubbles from nucleation sites. As the gas phase bubble detaches from the wall a void is left behind which the surrounding cool liquid phase rushes to fill. This agitation of the liquid phase, combined with the forced disruption of the thermal boundary layer near the wall

brings in cooler liquid from further afield. The heat transfer due to quenching is therefore higher than the standard convective heat transfer coefficient previously covered:

$$q_Q = h_Q A_Q \left(T_{wall} - T\delta \right) \tag{2.65}$$

The quenching heat transfer coefficient is obtained though empirical correlation from Del Valle and Kenning, assuming the bubble departs the wall normal to the surface [36].

$$h_Q = 2k_w f_{dep} \sqrt{\frac{t_w}{\pi \left(\frac{k_w}{Cp_w \rho_w} \right)}} \tag{2.66}$$

where k_w and t_w are the thermal conductivity of water and the waiting time between bubble departures.

Kurul and Podowski theorized that the waiting time between bubble departures accounts for 80 percent of the time of departure frequency [35]:

$$t_w = \frac{0.8}{f_{dep}} \tag{2.67}$$

The departure frequency itself is approximated as a function of vapour and gas properties. Cole presented this function based on a force balance on a bubble departing the surface in a quiescent pool. It does not necessarily apply to forced convection conditions, where bubbles will depart more readily, but is widely used nonetheless [37].

$$f = \sqrt{\frac{4\,g\Delta\rho}{3d_{dep}\rho_l}} \tag{2.68}$$

Tolubinski and Kostanchuk's correlation for liquid water and water vapour bubble departure diameter is based off of empirical fitting [38].

$$d_{dep} = min \left(0.0014 \,,\, 0.0006 \exp \left(\frac{T_{wall} - T_{sat}}{45} \right) \right) \tag{2.69}$$

The nucleation site density is a function of wall super heat, increasing as the surface gets hotter and hotter [39].

$$N = 210^{1.805} \left(T_{wall} - T \right)^{1.805} \tag{2.70}$$

Finally, the evaporation heat flux is the energy associated with the phase transition from liquid to vapour. This flux is proportional to the mass of water converted from liquid

to vapour and is calculated from this mass balance. Each bubble is assumed to be a perfect sphere with a diameter given by the bubble departure radius, therefore the volume may be calculated which combined with the vapour phase density gives the mass of each bubble. In conjunction with the heat of vaporization along with the frequency of departure and number of nucleation sites this yields the energy flux required for phase change. As the overall heat flux increases and the degree of superheat increases, more nucleation sites activate and the rate of boiling and heat transfer increases.

$$q_e = \frac{\pi}{6} d_{dep}^3 \rho_v f_{det} N \Delta H_{vap} \tag{2.71}$$

2.6 Numerical Coupling

The operation of a WHB is characterized by the interaction of two separate domains, the tube and shell side. In order to best represent this system, both sides should be considered, yet depending on the process conditions this can present a significant challenge. If the time scales of the two sides differ significantly, the numerical solution of both sides in tandem becomes computationally prohibitive since the time step will be governed by the smallest time scale. Various approximations have been proposed to alleviate this difference in scale.

Huaishuang et al. investigated the operation of a WHB both numerically and experimentally. They modelled a small system with 31 tubes, using hot exhaust air in the tube side to boil liquid water within shell side. To approximate the multiphase flow on the shell side of the WHB the drift flux model was used. The drift flux model is a simplification of two phase flow that treats the two phases as a single mixture with varying properties depending on the phase fraction. It is less computationally expensive than the two fluid model, but requires a priori knowledge of phase mixture properties and is not ideal for systems with varying relative velocities between phases. On the other hand the tube side was predetermined by using the experimentally obtained inlet and outlet exhaust air temperatures. The temperature of the exhaust air within the tubes was then assumed to decrease linearly from the observed inlet and outlet temperatures, subsequently the heat flux was set to decrease linearly proportional to the temperature difference between tube and shell side while averaging out to the observed heat flux. Good agreement between the model and the experimental system were observed, with the model matching the vapour production of the experiment within 10%. It was observed that the void fraction of the fluid was the largest factor in determining the heat transfer coefficient of the shell side [40].

Junjie et al. also approached the numerical solution of both the shell and tube side of a shell and tube heat exchanger. In order to reduce the computational load of the simulation,

a hybrid 1,2,3-D approached was used. The tube side was modelled with a cylindrical co-ordinate system and was split into two separate regions, the reaction zone and the non-reaction zone. At the inlet of the reaction zone a burner was present, this resulted in significant radial changes in flow properties and as such a 2-D axial symmetric simulation was solved assuming that the result was independent of the theta co-ordinate. After some distance past the burner and the end of the flame the model was simplified to a 1-D equation which assumed perfect radial mixing and only solved an energy balance between tube and shell side. In contrast to the tube side, the shell side was numerically solved using a full 3-D simulation, but rather than resolve the flow around each individual tube the tube bundle was approximated as a porous media. This added a secondary pressure drop across the tube bundle but arguably lost much of the surface effects responsible for heat transfer. Comparison with experimental results were favourable expect for poor agreement between the simulated and observed tube wall temperature distribution [41].

Sun and Yang used computational multiphysics to analyze the effect of support structures for tube bundles within a steam generator. A single tube with a u-bend was modelled, including the internal single phase domain, the solids dividing each domain, and the multiphase domain outside the tube. The two-fluid model along with the heat flux splitting methodology outlined in previous sections was used to approximate the shell side while standard Navier-Stokes was used to describe the tube side flow. Turbulence models were used in both domains and drag, lift, lubrication, and turbulent dispersion force closures were used within the multiphase domain. As both domains had similar flow rates and velocities, the time scales needed to solve each were comparable such that the two were solved with simultaneous coupling at the end of each time step. Steam quality at the outlet reported from the simulation agreed with plant data, and possible issues of recirculation at the end of the support structures were raised [42].

Wang et al. performed similar work with Ansys CFX in the simulation of a steam generator for nuclear power production. The system approximated numerically was a tube bundle with boiling multiphase flow in the channels between tubes, and single phase flow within the tubes themselves. Due to the triagonal spacing of the tube bundle, the authors modelled a triangle, the corners of which contained a wedge of a tube each. The edges of the triangle were resolved with a symmetrical boundary condition in order to represent a large system of multiple tubes. Coupling between each domain was done within each solution iteration due to the similar time scales in the two systems. Following comparison with experimental data by Bartolomei for a 2-D case of wall boiling, the thermal-hydraulic characteristics of the system were found to vary depending on the inlet subcooling and a low degree of subcooling was recommended for optimal heat transfer [43].

2.7 Numerical Solver

This work was performed using the `OpenFOAM` package. Built around a finite volume approach `OpenFOAM` has many in-built solvers for numerically solving various governing equations depending on the physics at play in the system [44]. When numerically solving the Navier Stokes equations with a finite volume method, the Gaussian integration across a computational element requires the values of flow parameters along the surfaces. The method chosen to compute these surface values has a large impact on the accuracy and stability of the simulation. Generally more stable discretization schemes such as upwind (1st order) are more numerically diffuse and of lower order. On the other hand higher accuracy schemes such as central difference are second order, but become unstable as flow becomes more convective in nature (higher speed flows) [9].

The central difference scheme (CDS) for a 1-D uniform spacing structured grid for the variable ϕ is as follows:

$$\phi_{i+1/2} = \frac{\phi_i + \phi_{i+1}}{2} \tag{2.72}$$

While the upwind scheme is:

$$\phi_{i+1/2} = \phi_{upwind} \tag{2.73}$$

where $\phi(i)$ denotes the central node value at cell i, $\phi_{i+1/2}$ is the value at the face of interest, and ϕ_{upwind} is the central node value directly upwind of the face (e.g. $\phi_{upwind} = \phi_i$ if $V > 0$ and $\phi_{upwind} = \phi_{i+1}$ if $V < 0$).

In order to balance accuracy and stability, it is very common to switch between discretization schemes locally depending on the flow configuration in nearby cells. For example using CDS in the bulk of the domain, and switching to upwind in areas of rapid change. When to and how to switch between schemes gives rise to the limiter function. Continuing the above example of a CDS, using a limiter to switch between an upwind or CDS solution yields the following:

$$\phi_{i+1/2} = \phi_{upwind} + l(r)\frac{-\phi_{upwind} + \phi_{downwind}}{2} \tag{2.74}$$

where $r = max\left(\frac{\phi_i - \phi_{i-1}}{\phi_{i+1} - \phi_i}, 0\right)$ and $l(r)$ is the limiter which is 1 when off and approaches 0 as it turns on.

The linear upwind difference scheme is similar in construction to the central difference scheme (LUD) and also second order, but rather than interpolate between two nodes it extrapolates forward from the two nodes upwind. Including a limiter to revert to upwind under high gradients, the LUD scheme is as follows:

$$\phi_{i+1/2} = \phi_{upwind} + l(r)\frac{\phi_{upwind} - \phi_{up-upwind}}{2} \tag{2.75}$$

where $\phi_{up-upwind}$ is the central node value of the twice upwind from the face (e.g. if flow is from node i to i+1 then $\phi_{up-upwind} = \phi_{i-1}$).

Multiple limiters are available for use, two will be used within the scope of this work. The first is the `OpenFOAM` limited scheme which is `OpenFOAM`'s default:

$$l(r) = max\left(min\left(2r\,,\,1\right)\,,\,0\right) \tag{2.76}$$

The second is the VanLeer approach [45]:

$$l(r) = \frac{r + |r|}{1 + r} \tag{2.77}$$

Chapter 3

Tube-Side Model and Simulations

In a waste heat boiler (WHB) the temperature differential between the hot process gases and the cooler boiler water drives heat transfer. Flow within the tube portion of the WHB is driven by the reaction furnace upstream and is less dependent on the heat transfer that occurs between the two domains when compared to the shell side in which boiling occurs. Therefore, the tube side of the process is first simulated before approaching the shell side. The geometry of the system along with the process conditions modelled are discussed, followed by the methodology in their implementation. Finally, results are presented and compared to a typical empirical formulation used for turbulent heat transfer in internal flows.

3.1   Geometry and Process Conditions

The tube-side domain geometry modelled in this work consists of four separate materials, three solids and a fluid. The fluid is the process gas exiting the reaction furnace containing hydrogen sulphide, sulphur dioxide and nitrogen, and the solids are the metal of the tubesheet and tube itself, the ceramic ferrule, and the insulating ceramic fibre-based "paper" in between the ferrule and metal. Material properties vary widely from material to material, for example in density and thermal conductivity. All material properties used in the simulation for each region are specified in table 3.1.
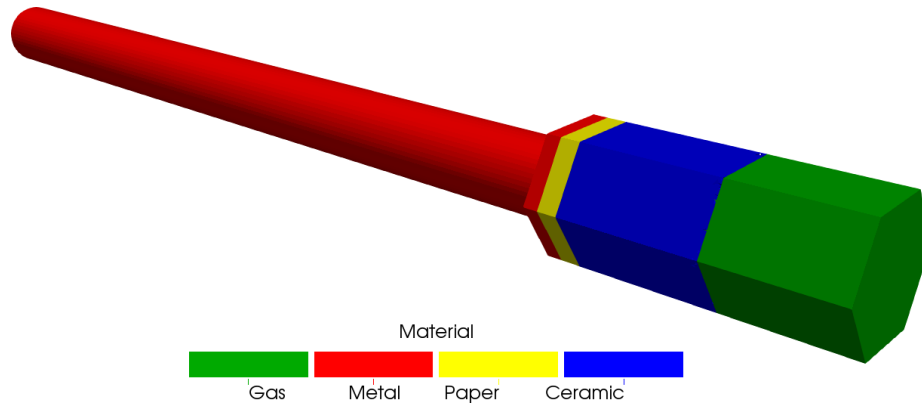
Figure 3.1: Schematic of the tube-side geometry with sub-domain materials indicated.
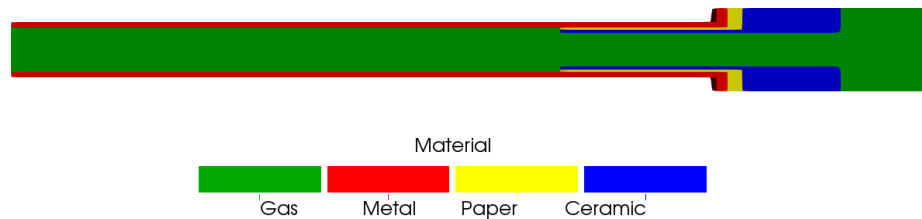

Figure 3.2: Inner cross section of tube side domain. Notice how the ferrule inserts into the metal tube and the backwards facing step as the ferrule ends.

Material	Density (kg/m^3)	Thermal Conductivity $(W/m.K)$	Viscosity $(Pa.s)$	Heat Capacity $(J/kg.K)$
Process Gas	1	0.026	1.5×10^{-5}	1216
Metal	7833	54	-	565
Ceramic	2595	3.5	-	1000
Paper	140	0.24	-	700

Table 3.1: Material Properties of the Tube-Side Geometry.

A schematic of the geometry the tube-side geometry is shown in Fig. 3.1. Further detail of the geometry is shown in the domain cross-section, Fig. 3.2.

The ceramic portion (blue) is known as the ferrule, it is an insulator for the metal surfaces which are being protected from the elevated temperatures of the process gas. These elevated temperatures promote both corrosion and lower the mechanical modulii of the

metal. Furthermore, the ceramic acts as structural support for the insulating ceramic fibre paper material. The paper material (yellow) serves as the main insulating component protecting the metal, lowering the metal temperatures at the inlet where the process gas temperatures are the highest. The metal tube (red), composed of stainless steel, includes the tube and tubesheet which form the interface between the shell and tube side simulations. Finally, the process gas (green) is the only fluid domain in the tube side simulation, which transports thermal energy down the length of the tube.

The system modelled is typical of a WHB with a hexagonal tube spacing and a flush welded tube sheet. The total length of the system modelled is $834\,mm$ and the hexagonal portion is $75\,mm$ from top to bottom (line centre to line centre). Measured from inlet to outlet the ceramic ferrule is $254\,mm$ long, the metal extends $500\,mm$ past the outlet of the ferrule and the inlet region is $80\,mm$ long. The ferrule has an outer and inner diameter of $36\,mm$ and $30\,mm$ respectively compared to $50\,mm$ and $40\,mm$ for the metal. Finally, the tube sheet, paper gasket, and hexagonal portion of the ferrule are $10\,mm$, $13\,mm$, and $89\,mm$ thick respectively. A summary of all the geometrical dimension may be found in table 3.2.

Dimension	Distance (mm)
Ferrule Length	254
Metal Length	652
Inlet Length	80
Hexagonal Height	75
Ferrule ID	30
Ferrule OD / Paper ID	36
Metal ID / Paper OD	40
Metal OD	50
Paper Gasket Thickness	13
Tube Sheet Thickness	10
Hexagonal Ferrule Portion Thickness	89
Ferrule Inlet Fillet Radius	5

Table 3.2: Dimensions of Simulation Domain

The external boundaries of the tube side simulation are displayed in Fig. 3.3 and Fig. 3.4. There is the inlet face where the process gas enters the domain, and symmetry boundaries associated with the geometry. Furthermore, the shell-side boundary is the interface between the shell and tube side simulations, with heat transfer occurring between
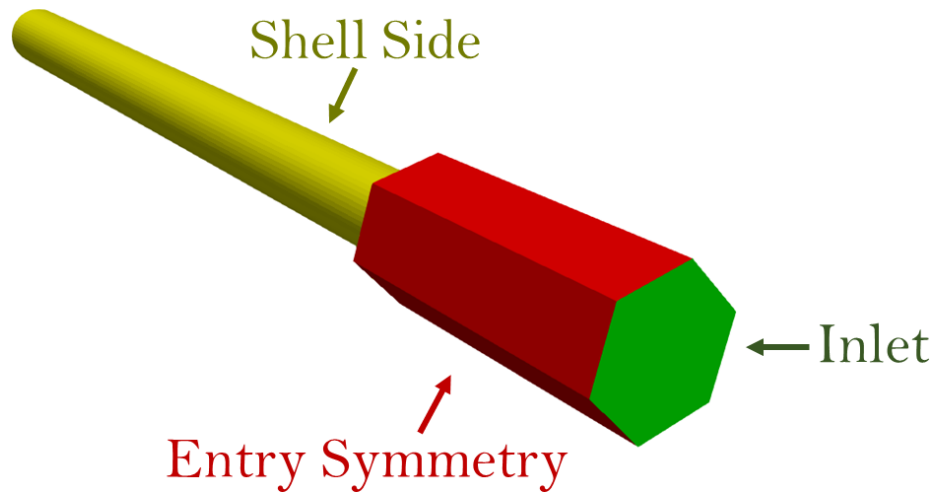
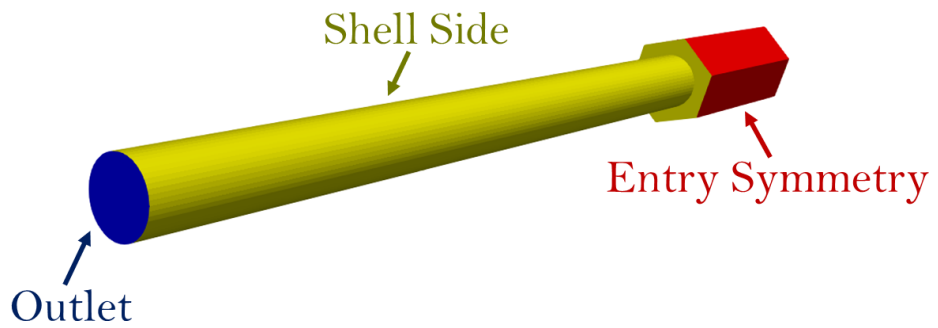Figure 3.3: Boundary Faces of Tube Side Domain Viewing from Inlet

Figure 3.4: Boundary Faces of Tube Side Domain Viewing from Outlet

the two. Finally, the outlet of the domain is extended to allow for outlet flow to develop with zero-gradient boundary conditions being used. The boundaries applied to each of these surfaces will be reviewed in section 4.2.

3.2   Model

In order to numerically solve the Navier-Stokes equations for flow, boundary conditions need to be applied to the multiple physical surfaces which define the simulation domain. This in turn requires assumptions and simplifications to represent the physical boundary, which may act as an error source for the simulation. There are two types of surfaces in the simulation: internal which represents interfaces between different materials in the simulation, and external which are the edges of the computational domain. When first considering solely the fluid flow, there are four separate groups of surfaces which encapsulate the different boundary conditions to resolve the flow profile, one internal and three external.

First is the outlet, an external boundary, of the ferrule system simulation. The outlet region has been extended past the end of the ferrule in order to allow the flow to fully develop after exiting the ferrule itself. This is of relevance as some flow properties and assumptions must be made at the outlet, and flow must be fully developed for these to be valid, otherwise the solution will be over constrained providing poor results. Assuming flow is fully developed at the outlet of the simulation, the boundary condition for the fluid velocity is one of a zero gradient normal to the outlet.

The fluid pressure at the outlet surface is explicitly specified (Dirichlet boundary condition) to be at atmospheric pressure, as gravitational forces are not considered in the simulation and flow is in-compressible, pressure should not vary in the radial direction.

$$n_S \cdot \nabla \boldsymbol{V} = (0\,0\,0)\ s^{-1} \tag{3.1}$$

$$P = 101300\ Pa \tag{3.2}$$

Proceeding upstream from the outlet, the next boundary encountered is the internal surfaces in which the fluid contacts the solid walls of the pipe and ferrule. A Dirichlet boundary condition of zero is set to the velocity along these surfaces as the fluid-wall interface is a no-slip condition. No flow is allowed to penetrate the wall and, as such, there is no momentum flux through the wall. Solving Eqn. (2.2) in the direction normal to the wall shows that without a momentum flux, there is no pressure gradient along this normal.

$$n_S \cdot \nabla P = 0\ Pa/m \tag{3.3}$$

35

$$\boldsymbol{V} = (0\ 0\ 0)\ m/s \tag{3.4}$$

Further upstream there is the external entry zone to the ferrule, this region extends out a fair distance from the inlet of the ferrule. There is uncertainty in the flow profile introduced at the inlet of the simulation domain, by extending this inlet region room is given for the uncertainty to relax to an organic flow profile given the geometry. The surfaces bounding this region have normals orthogonal to the mean direction of flow and the velocity component normal to the surface has been set to zero. Similarly to the wall surfaces, since there is no momentum flux through the entry zone, the gradient of pressure normal to the entry zone surface is also zero.

$$n_S \cdot \boldsymbol{V} = 0\ m/s \tag{3.5}$$

$$n_S \cdot \nabla P = 0\ Pa/m \tag{3.6}$$

Finally, there is the external inlet boundary to the simulation. Flow properties at this point are uncertain, as flow is originating in a reactor furnace with a large burner. Likely flow is quite turbulent and non uniform, in order to best represent the "average" ferrule and tube, the overall volumetric flow rate for the tube side of the WHB was divided equally between all tubes. Process data from the industrial partner Industrial Ceramics Ltd. detailed a system of 180 tubes processing $10.5\ m^3/s$ of flow. The resulting flow rate was then converted to a plug flow velocity profile at the inlet leading to the following condition:

$$\boldsymbol{V} = (0\ 0\ -12)\ m/s \tag{3.7}$$

Considering that there is a slip/symmetry boundary condition throughout the inlet region and that this region is well extended from the inlet of the ferrule proper, it was assumed that there is a lack of viscous forces which would induce a pressure drop along the main axis of flow. Hence the pressure boundary condition at the inlet was set to a Neumann condition with a gradient of zero.

$$n_S \cdot \nabla P = 0\ Pa/m \tag{3.8}$$

The turbulence properties ω and k were handled using Menter's recommended boundary conditions [19]. As velocity approaches zero at the walls due to the no slip boundary condition, flow transitions from turbulent to laminar. Following this profile, the turbulent kinetic energy will decay to zero at the wall, and this was the boundary applied in the

simulation. For ω, the boundary is not as straight forward since the specific rate of dissipation is undefined at the wall due to k decaying to zero. The boundary condition used for this model is as follows:

$$k_{wall} = 0 \ m^2/s^2 \tag{3.9}$$

$$\omega_{wall} = 10\frac{6\nu}{\beta_1(\Delta d_1)^2} \ s^{-1} \tag{3.10}$$

where $\Delta d_1 = $ distance from nearest wall and $\beta_1 = 0.075$.

At the outlet it was assumed flow would be sufficiently developed due to the extended region of metal tube that there would be no gradient in k or ω as they approached the outlet surface.

$$n_S \cdot \nabla k = 0 \ m/s^2 \tag{3.11}$$

$$n_S \cdot \nabla \omega = 0 \ s^{-1}m^{-1} \tag{3.12}$$

Equation (3.12) and Eqn. (3.11) also apply to the inlet region for the turbulent properties in order to allow them to develop before reaching the mouth of the ferrule. At the inlet surface of the simulation domain the turbulent properties are specified via the following Dirichlet conditions:

$$k_{inlet} = \frac{3\left\|\boldsymbol{V}_\infty\right\|^2 I^2}{2} \ m^2/s^2 \tag{3.13}$$

$$\omega_{inlet} = \frac{k_{inlet}^{0.5}}{l} \ s^{-1} \tag{3.14}$$

k is determined by taking assuming the inlet turbulence intensity to be equal to 5%, which corresponds to a moderately turbulent flow, the value for k is then computed via the definition of turbulence intensity. ω is resolved through the mixing length model using the spacing in-between two tubes as the characteristic length of flow.

With regards to temperature, the condition at the inlet surface of the simulation is a Dirichlet condition. Based on a standard process provided by the industrial partner, the outlet temperature of the reaction furnace ($1400 \ K$) was set as the inlet temperature to the simulation.

$$T_{inlet} = 1400 \ K \tag{3.15}$$

Similar to the turbulent properties, the temperature boundary at the slip surfaces of the inlet region is symmetrical. While there should be some small gradient in temperature at the outlet surface, due to the continued cooling of the process gas, the gradient in temperature was forced to zero normal to this surface for numerical stability.

$$n_S \cdot \nabla T = 0 \ K/m \tag{3.16}$$

Finally, at the walls the heat transfer is determined via the Reynolds analogy which assumes that the same turbulent eddies responsible for momentum flux near the walls also govern the transfer thermal energy [46].

$$q = h\left(T_{wall} - T_{\delta}\right) = \frac{\boldsymbol{\tau_W}\, C_p}{u_{\delta}}\left(T_{wall} - T_{\delta}\right) \tag{3.17}$$

where $\boldsymbol{\tau_W}$ is the viscous stress at the cell node nearest to the wall, u_{δ} the velocity at the nearest node, and T_{δ} the temperature at the centre of the nearest node.

This concludes specification of the boundary conditions for the fluid domain of the tube-side geometry. In the solid domains only the energy equation is solved so boundary conditions are only needed for the temperature. Along any surface in which one region encounters the other the fluxes and temperatures at the faces are set equal.

$$T_{s1} = T_{s2} \tag{3.18}$$

$$\boldsymbol{q}_{s1} = \boldsymbol{q}_{s2} \tag{3.19}$$

Along the surfaces which form a external hexagonal perimeter of the simulation, near the inlet to the ferrule, an insulating condition has been set due to symmetry in the larger physical system, following Eqn. (3.16). Finally, the external surfaces which contact the boiler water along the shell side of this wider work are initially solved using a heat transfer coefficient and far field temperature, solving the heat via Eqn. (3.20):

$$q_s = h(T_{wall} - T_{\infty}) \tag{3.20}$$

where h and T_{∞} were set to $5750\,W/m^2.K$ and $523\,K$, respectively.

The boundary conditions for the fluid phase mentioned and their implementation in `OpenFOAM` are summarized in table A2 in Appendix 1.

`OpenFOAM` allows for different discretization schemes to be applied to each conserved variable across the simulation. As the simulations presented occur in a highly turbulent regime, the discretization of different terms generally prioritizes stability and boundedness when possible, while keeping the accuracy above first order. The schemes used for different terms are summarized in table 3.3.

The solver used for this portion of the work was chtMultiRegionSimpleFoam, which is capable of handling both fluid and solid regions with coupled boundaries. Within the solid regions chtMultiRegionSimpleFoam solves Eqn. (2.6) while for an incompressible fluid it

Variable	Discretization	Limiter
Velocity	CDS	linear
Enthalpy	CDS	linear
Pressure	CDS	linear
κ, ω	CDS	linear

Table 3.3: Finite Volume Discretization Scheme Applied in `OpenFOAM`

solves Eqns: 2.4, 2.1, and 2.2 via the SIMPLE algorithm. SIMPLE stands for semi-implicit method for pressure linked equations, and is an iterative approach for solving the steady state Navier-Stokes equations. The SIMPLE algorithm consists of first applying the boundary conditions to domain, after which the discretized momentum equations are solved to compute the guessed velocity field along with the mass fluxes at each face. Using these results, the pressure corrector is solved for using the pressure equation, and the mass fluxes re-evaluated, looping between these two steps consists of the "inner loop" and can be iterated repeatedly to correct for non-orthogonality between cells. Once the pressure field is updated, the velocity field is corrected and boundaries updated, at this point energy, turbulence, or any other equations are solved and then the process whole process is repeated until some desired convergence is reached [20].

In order to accelerate convergence, for the first thousand SIMPLE iterations the energy equation was omitted and only the flow field solved. As the material properties are assumed to be independent of temperature, the solution could be decomposed in this way since there is no temperature dependency in the flow. With the flow profile converged, the heat equation was then introduced and solved to convergence.

Great care was taken with the construction of a fully structured mesh throughout the entire tube side domain. As shown in Fig. 3.5 the mesh is complete with boundary layer elements where the elements nearest to the wall become progressively thinner and thinner in the direction normal to the wall. This is of particular importance when computing turbulent flow since as the flow slows in proximity to the wall due to the no slip boundary condition, the length scale and intensity of turbulence decreases. The $k-\omega$ SST turbulence model used resolves turbulence all the way to the laminar sublayer and for this purpose requires very fine mesh elements in close proximity to the wall. There are 6.2 million hexahedral fluid elements in the mesh used along with 190 thousand solid elements.
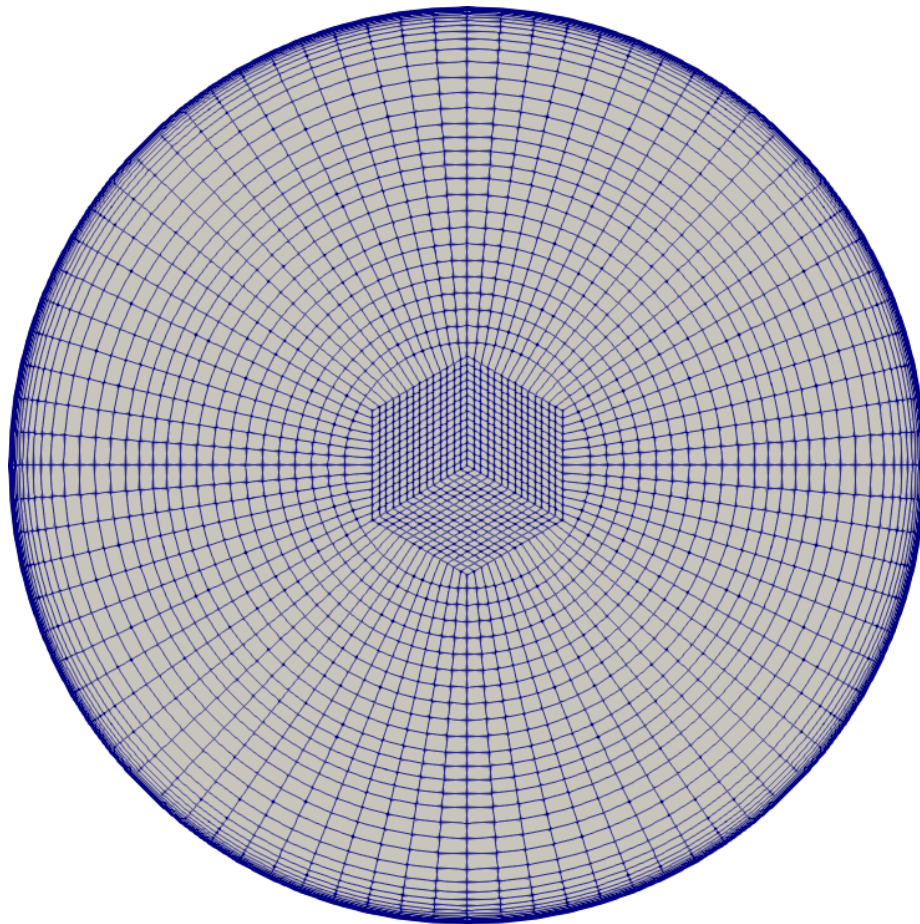
Figure 3.5: Mesh at the outlet of the tube-side domain, fully structured with wall boundary layer elements and a hexagonal core.

3.3 Results Discussion

With the methodology outline above, the steady-state solution computed complies with expectations and previous industrial collaborator experience. As visible in Fig. 3.6 and Fig. 3.7 flow travels from right to left through the fluid domain; these two figures only illustrate the fluid domain as the velocity and pressure flow variables are only pertinent to the fluid. Initially, flow within the inlet region is slow relative to further down stream, and there is a high pressure head. Furthermore, through the first half of the inlet region there are no visible changes in the flow pattern, indicating that this region is long enough to not over constrain flow as it approaches the ferrule inlet. As flow enters the ferrule throat, it accelerates due to the reduction in the cross-sectional area of the flow channel. Through the ferrule the bulk velocity of the fluid is at a peak, this has the effect of reducing pressure to a minimum as potential energy is converted to kinetic energy.

As flow exits the ferrule, it encounters a sudden dilation in the flow channel. This promotes a jet like behaviour at the outlet and the development of a recirculatory region next to the ledge created by the end of the ferrule. The recirculation zone is typical of backward facing steps in RANS turbulence simulations [47]. There is a significant amount of churning and viscous stresses in this recirculation zone which generates a large amount of turbulent kinetic energy as Fig. 3.8 shows. Once the flow enters the larger diameter pipe, it begins to slow at which point the pressure rebounds as kinetic energy is again converted back to potential. The pipe extends 25 tube diameters past the outlet of the ferrule, allowing the flow ample room to fully develop, which occurs around 13 diameters in. Therefore, the outlet boundary condition is demonstrably not overly constraining the solution near the outlet of the ferrule.

Figure 3.9 and Fig. 3.10 demonstrates the effect of the ferrule system in maintaining a cool metal surface. Most of the temperature gradient occurs through the paper insulation which is to be expected as a result of its thermal conductivity being less than one two-hundredth that of the metal and an order of magnitude less than that of the ceramic. Therefore, in order to maintain the same heat flux the gradient in temperature of the paper must be roughly two hundred times greater than in the metal if one were to consider a 1-D Cartesian approximation.
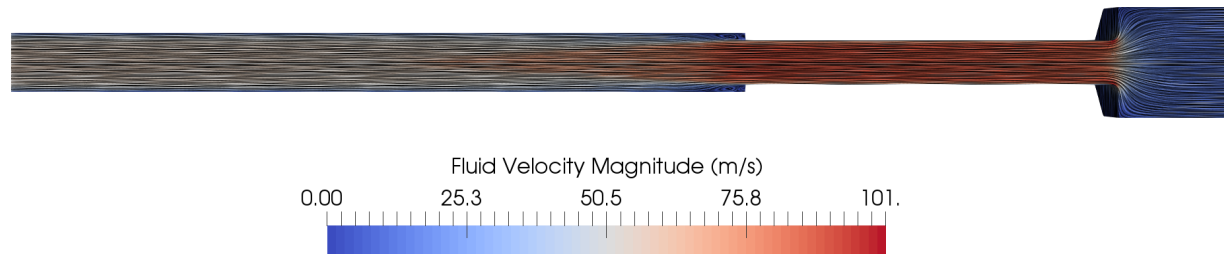
Figure 3.6: Cross sectional velocity profile overlayed with streamlines, recirculation is visible at the outlet of the ferrule and otherwise flow is fairly unidirectional.
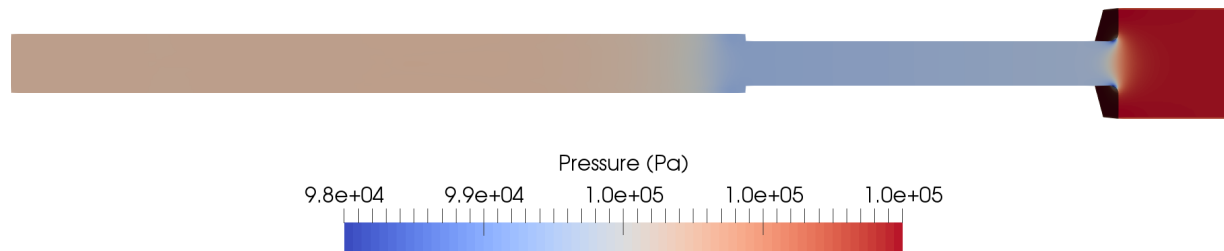

Figure 3.7: The cross sectional pressure profile illustrates the anticipated pressure drop through the ferrule and subsequent pressure increase.
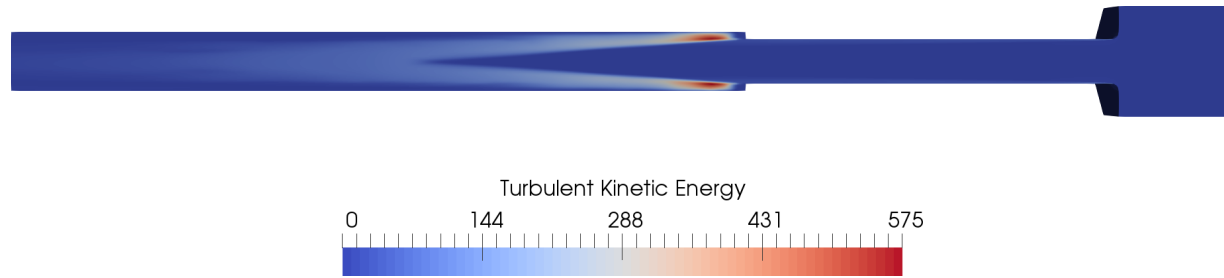
Figure 3.8: The cross sectional turbulent kinetic energy visualization demonstrates the high amount of turbulent energy generated within the recirculation zone that then propagates down stream.
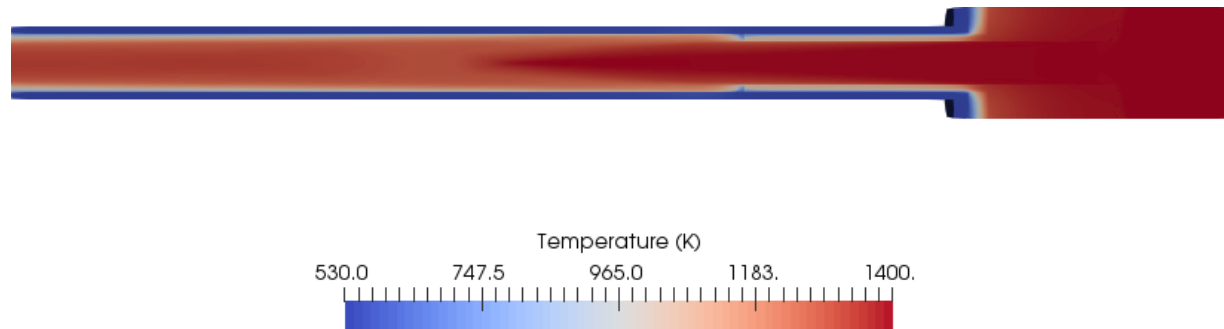

Figure 3.9: The cross sectional temperature profile shows the gradual cooling of the process gas, particularly after the ferrule, and a thin thermal boundary layer next to the solid walls.
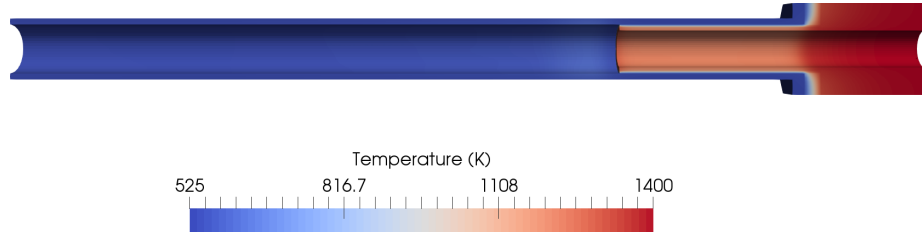
Figure 3.10: From the cross sectional solid temperature profile it is evident that the ferrule system is keeping the metal much cooler than the process gas.

Of note is the elevated temperatures after the ferrule, particularly as the the recirculation zone ends and the flow reattaches with the wall. At this impingement point, the flow approaches the near wall with a significant portion of velocity normal to the wall when compared to fully developed flow. This reduces the thickness of the viscous sub-layer and also advects higher temperature fluid from the bulk flow into close proximity of the wall. These two effects work in tandem to significantly increase the heat transfer and create a localized hot spot on the metal tube. Figure 3.11 clearly demonstrates this point along with the benefits of a full computational multiphysics simulation of the tube side as opposed to an empirical correlation such a Sieder Tate [6]. The hot spot extends to the outer surface of the pipe as well as seen in Fig. 3.12, which will have a noted impact on the subsequent shell side simulation as this surface is the physical boundary between both domains.

The added insight provided by a simulation is very useful for a system such as this, as for example the temperature at the hottest point of the metal in contact with the fluid is over $60\,K$ hotter than the temperature predicted via the Sieder-Tate correlation. In a system such as this, where failures are localized as opposed to occurring at bulk conditions, localized results aid in design and sizing.

$$St = 0.023 Re^{-0.2} Pr^{\frac{-2}{3}} \left(\frac{\mu_b}{\mu_W} \right)^{0.14} \tag{3.21}$$

$$St = \frac{h}{\rho C_p \left\| \boldsymbol{V}_b \right\|} \tag{3.22}$$

where Pr is the Prandtl number, the subscripts $_b$ and $_W$ are variables in the bulk and at the wall respectively.

The Sieder-Tate approximation was used to compute the heat transfer coefficient along the surface of the inner tube diameter. Heat flux through the tube and expected tube
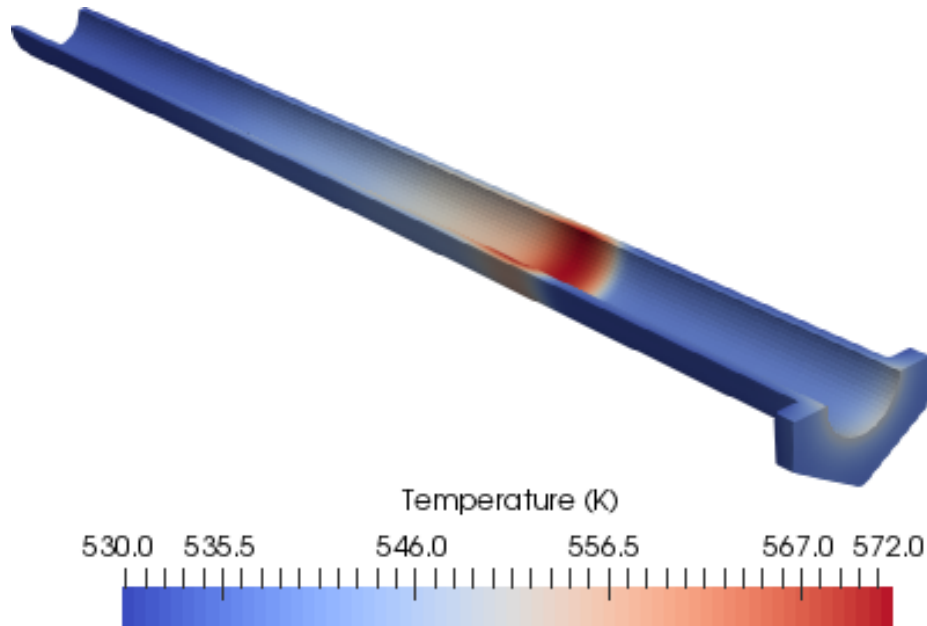
Figure 3.11: The cross sectional metal temperature profile illustrates the pronounced impact that the recirculation zone has on the metal temperature.

surface temperatures were then solved for with a thermal resistance in series approach. In this calculation the heat transfer coefficient on the tube inner diameter was paired with the inlet process gas temperature in Eqn. (3.20), heat diffusion through the shell was approximated via radial heat conduction governed by Fourier's law, and the tube outer diameter governed by Eqn. (3.20) where h was $5750 \, W/m^2.K$ and T_∞ was $523 \, K$.

When the results obtained are compared to the Sieder Tate correlation for turbulent flows, Eqn. (3.21), it was found that temperatures well downstream of the ferrule (when flow is fully developed) the surface temperatures of the walls are notably cooler than predicted. The outer pipe wall was found to be $535 \, K$ in the simulation compared to the $543 \, K$ predicted by Sieder-Tate, similarly the inner temperatures were $544 \, K$ compared to $554 \, K$. Heat flux through the wall is 18% lower in the simulation, at $13.7 \, kW/m$ against 16.8 kW/m. Possible reasons for this discrepancy is first, with a Prandtl number of 0.7 fluid properties are on the edge of validity for Sieder-Tate, secondly as an empirical correlation, Sieder Tate is not expected to be highly accurate.

Certain deficiencies exist within the presented simulation, namely fluid parameters are assumed to be constant within the entire domain, but given the large changes in temperature and pressures it would be more appropriate to use variable viscosity, density,
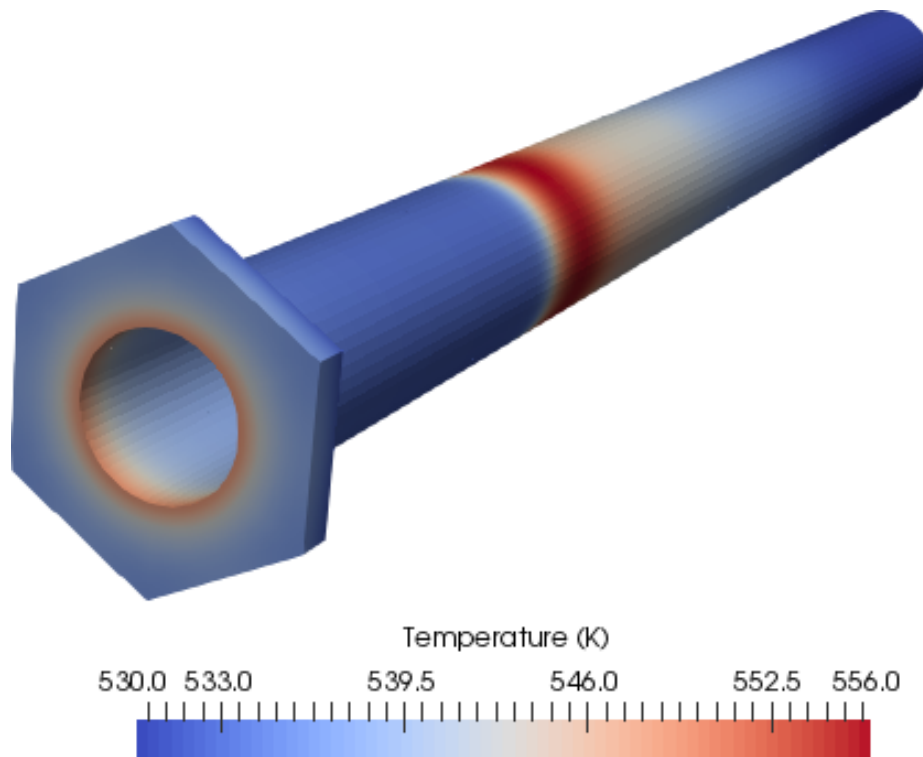
45

Figure 3.12: The metal temperature on the outer surface of the ferrule peaks near the recirculation zone, along with at the inlet to the metal tube.

thermal conductivity, and heat capacity. These changes would improve model fidelity, particularly near the wall layers where there is a pronounced temperature change as the fluid approaches the wall. Other points of improvement include using a more advanced turbulence model, possibly a Reynolds stresses approach. All two equation turbulence models rest on the assumption of isotropic turbulence, which for free streams is quite justified. Due to the no slip condition at the wall, in proximity to the wall before turbulent eddies dissipate completely they are not isotropic as they do not approach the wall [11]. This is a well known limitation of two equation models, which tend to build up excessive turbulent kinetic energy in stagnation points and recirculatory zones.

Reynolds stresses models, rather than assuming turbulence is isotropic like viscosity, computes 9 equations resulting in much higher computational costs, one for each component in the turbulent stresses tensor. This allows for greater fidelity near the wall as turbulent stresses will predominantly fall in plane with the wall as opposed to normal to it. As heat transfer is dependent on the same eddies as momentum transfer from the bulk to the wall, higher accuracy turbulence near the walls implies higher accuracy in the heat transfer.

Chapter 4

Shell-Side Model and Simulations

The shell side portion of the waste heat boiler (WHB) cools the hot process gases travelling through the tube side through convective boiling. It achieves this by boiling purified water along the outer surface of the tubes, cooling the process gas via conduction through the metal tubes. This process takes advantage of the high latent heat of vaporization of water along with the high heat transfer coefficient associated with forced convection. By its nature, the boiling is dependent on the temperature difference between the shell and tube sides, therefore the shell side simulation is performed using the results of the previous section. First an overview of the simulation geometry is covered along with the geometric simplifications made to the overall system. Then the material properties of the two fluids is presented, and the boundary conditions used along each surface shown. This is followed by a brief overview of the numerics and mesh used, and finally the results of the simulation along with areas of possible improvement are discussed.

4.1 Geometry and Process Conditions

The shell side portion of the overall simulation of a WHB involves two phases, liquid water and water vapour. Using equations 2.43 and 2.44 where the vapour is the dispersed and the liquid is the continuous phase, the two are treated as interpenetrating continua which may be solved numerically using a single domain. Within industry, a WHB may contain any number of tubes ranging from tens to thousands, therefore simulating the full shell side would be not only computationally prohibitive, but also be particular to a single WHB. In light of this, only a subset of tubes is considered in this work. A periodic domain consisting
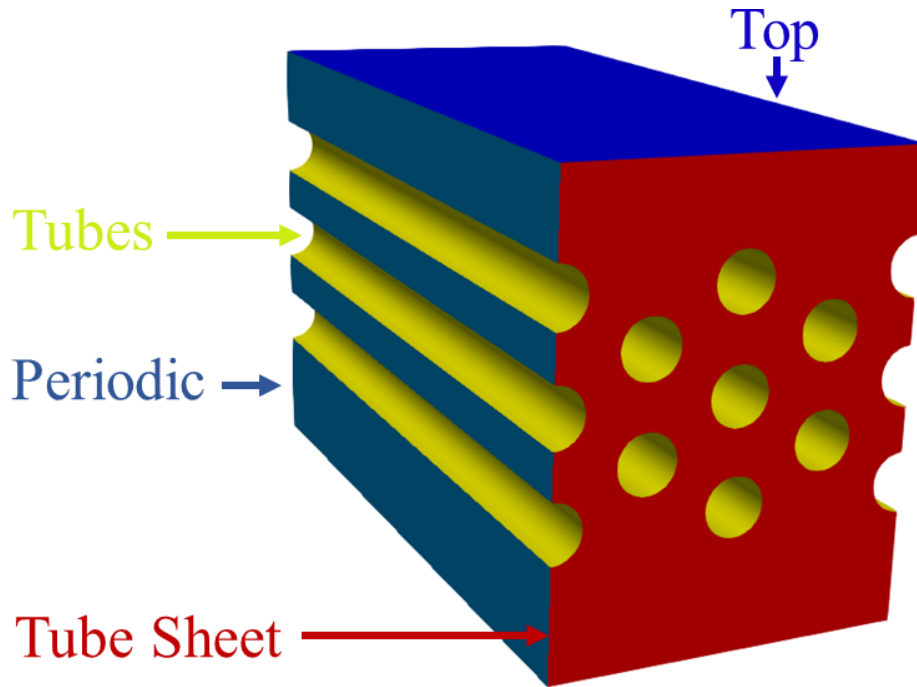
Figure 4.1: Schematic of the shell-side geometry with boundary labels: Red is the boundary defined by the tube sheet wall, yellow are the outer walls of the tubes, deep blue is the top outlet of the domain, and sky blue is the periodic boundary.

of 5 rows of tubes in a hexagonal pattern was chosen as a representative sub-unit of the shell side of a WHB.

Within the shell side, we expect flow to be complex and vary in all directions. This rules out the use of a less computationally expensive 1 or 2-D model, but some simplifications may be made for the sake of computational effort. By reducing the domain to a sample size of 10 tubes as seen in Fig. 4.1 and using a periodic domain the number of computing elements is greatly reduced. This approach ignores the effects of the shell walls, simulating 5 infinite rows of tubes, but considering most of the tubes are not on the periphery of the tube bundle the shell wall effects should be negligible for "bulk" tube conditions. As flow extends away from the tube sheet along the length of the tube (z-direction) it is expected that flow variables will become independent of this direction, therefore only a certain portion of the z-direction needs to be within the computational domain. The dimensions of the computational domain are found in table 4.1.

Flow enters the domain via the bottom surface, at this point the only phase present is
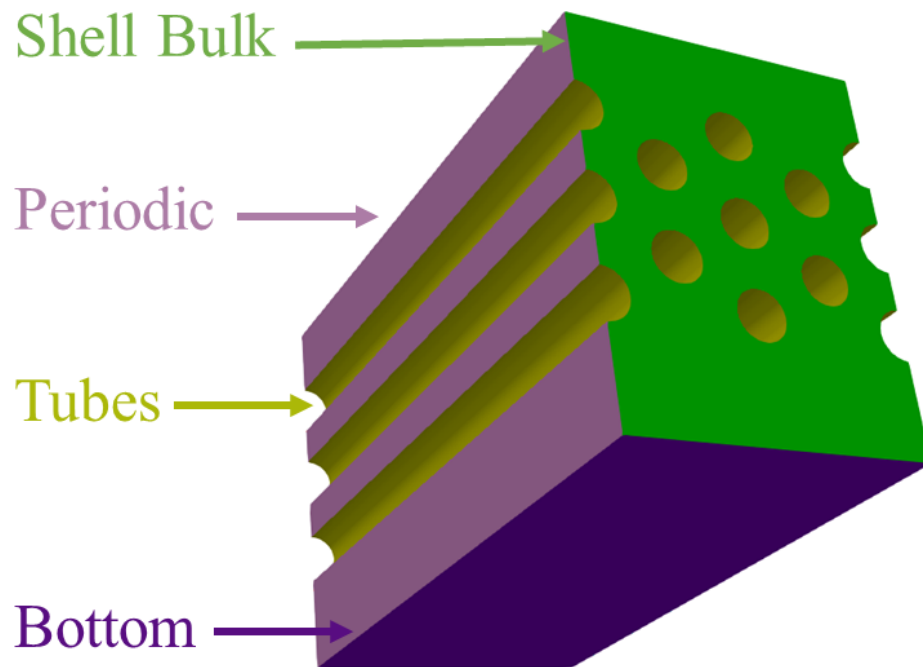
Figure 4.2: Schematic of the shell-side geometry with boundary labels: green is the boundary after which it is assumed the bulk conditions on the shell side do not vary along its length, light purple is the other half of the periodic faces, and in dark purple is the bottom inlet to the domain.

Dimension	Distance (mm)
Length of Tubes	642
Horizontal Length of Domain	300
Vertical Length of Domain	385
Tube Pitch	86.6
Tube Diameter	50

Table 4.1: Dimensions of Simulation Domain

liquid, cooled a few degrees below the boiling point. There is an entry region to allow flow to conform and develop before any changes in flow channel area. As flow travels upwards, it passes around the tube bundle, accelerating due to the contraction in flow cross sectional area. At this point it is also heated, and the dispersed gaseous phase is introduced at the tube surfaces due to phase-change. Finally flow, now containing both liquid and gas phases, approaches an outlet region above the tubes and then exits the domain via the top surface.

While there is only a single computational domain, two fluids flow within it, liquid water and water vapour. The material properties of both must therefore be specified in order to compute a solution to the governing equations. Table 4.2 summarizes the material properties input into the shell side simulation, of note is the density difference between the two phases. This will drive a buoyancy force on the gaseous phase which will accelerate relative to the liquid phase. Furthermore, the difference in enthalpy between the two phases determines the energy associated with phase change at these conditions, impacting the conversion of mass from liquid to gas at the boiling surface.

Property	Liquid	Gas
Density (kg/m^3)	789	16.3*
Viscosity ($Pa.s$)	$1.03 \cdot 10^{-4}$	$1.78 \cdot 10^{-5}$
Enthalpy (kJ/kg)	1120	2800
Heat Capacity Cp ($kJ/kg.K$)	4.95	4.21
Prandtl Number	0.831	1.41

Table 4.2: Material Properties of Liquid Water and Water Vapour at 40 bar and 530 K. * Calculated Using Ideal Gas Law

The simulation of the shell side covers the case of subcooled boiling. As outlined in section 2.5, it is assumed that all heat transfer from the heated surfaces to the fluid domain

contributes to one of three pathways: phase change, quenching, or convective heating. As such the gaseous phase is always assumed to be at the saturation point, namely the temperature is fixed as a function of pressure. The saturation temperature of the vapour is calculated using linear interpolation between the points provided in table 4.3.

Pressure (MPa)	Saturation Temperature (K)
3.75	519.73
3.80	520.51
3.85	521.27
3.90	522.03
3.95	522.78
4.00	523.53
4.05	524.27
4.10	525.00
4.15	525.72
4.20	526.44
4.25	527.15

Table 4.3: Water Vapour Equilibrium Temperature and Pressure

When solving the governing equations for multiphase flow, Eqn. (2.44) and Eqn. (2.43), one phase needs to be designated the dispersed and the other the continuous phase. In the case of this work is assumed that the liquid is always the continuous phase, and the gas phase is always dispersed, given that gas concentrations should on average be very low due to the heat fluxes and flow rates present. The diameter of the gas bubbles is treated as a constant $5\,mm$ for all momentum transfer calculations [48].

4.2   Boundary Conditions

In order to computationally solve the system at hand, boundary conditions need to be applied to each surface in the domain. For the inlet to the system, the overall flow passing though the shell side of the WHB was averaged between the cross sectional area along the vertical centre-line of the shell. This averaged velocity was applied to the bottom inlet for both the gas and liquid velocities.

$$\boldsymbol{V}_{l,g} = (0\ 0.0009\ 0)\ m/s \tag{4.1}$$

An inlet region is present within the computational domain, this allows flow to develop before encountering a tube which alters the flow profile. It is assumed that this region is long enough and there is a lack of viscous stresses (due to plug flow in this region) such that the dynamic pressure gradient is zero at the inlet.

$$\boldsymbol{n}_s \cdot \nabla P = \boldsymbol{n}_s \cdot \rho \boldsymbol{g} \; Pa/m \tag{4.2}$$

Along the sides that are periodic, the computational nodes along each edge are attached, therefore only the governing equations are solved along these surfaces. This represents a system which is infinitely long in the x-direction such that the rows of tubes are infinite.

Along the walls of the tubes and the tube sheet the liquid velocity is dictated by a no-slip boundary condition.

$$\boldsymbol{V}_l = (0\,0\,0) \; m/s \tag{4.3}$$

In contrast, along these same surfaces the gaseous phase is allowed to slip. Physically the gas phase does not slip along the surface at these process conditions, but the scale of this no slip behaviour is much smaller than the mesh elements at these points due to the lower viscosity of the gas phase. Furthermore bubbles are expected to roll across the surfaces and outside of nucleation points the liquid phase is always assumed to be wetting the surface. Some works [20], include wall repulsion forces into the momentum exchange terms in consideration of the liquid phase wetting, though such a term is not included in this work. To account for this non wetting and slip within an Euler-Euler framework, a slip boundary condition is applied to the gaseous phase velocity along the solid surfaces.

$$\boldsymbol{n}_{wall} \cdot \boldsymbol{V}_g = 0 \; m/s \tag{4.4}$$

In either case, no momentum flux is allowed through the wall, therefore there is no dynamic pressure gradient approaching the wall.

$$\boldsymbol{n}_s \cdot \nabla P = \boldsymbol{n}_{wall} \cdot \rho \boldsymbol{g} \; Pa/m \tag{4.5}$$

The shell bulk surface is not a physical surface, past this point the shell side continues for many more meters. Heat flux and boiling is present in this region as well, and as the process gas in the tube side cools travelling through the tubes, the heat flux through the tubes should lessen as the gas advances. The magnitude of this gradient in heat flux compared to the differences experienced at the outlet of the ferrule is quite small though, as visible in the tube section results. Therefore similarly to the tube side simulation this

shell bulk surface is treated as the point after which process conditions are constant when travelling in the surface normal direction. In line with this reasoning, a slip condition is applied at this point for both velocities, and the dynamic pressure gradient is set to zero.

$$\boldsymbol{n}_s \cdot \boldsymbol{V}_{l,g} = 0 \, m/s \tag{4.6}$$

$$\boldsymbol{n}_s \cdot \nabla P = \boldsymbol{n}_s \cdot \rho \boldsymbol{g} \, Pa/m \tag{4.7}$$

Finally at the outlet the pressure is fixed to the shell side pressure. There is also an outlet region to allow flow to fully develop after departing the tubes and therefore the gradient of velocity normal to the outlet surface is set to zero.

$$\boldsymbol{n}_s \cdot \nabla \boldsymbol{V}_{l,g} = (0\,0\,0) \, s^{-1} \tag{4.8}$$

$$P = 40 \, bar \tag{4.9}$$

The energy equation also requires boundary conditions in the form of heat fluxes or temperatures. At the bottom inlet flow the liquid is assumed to be 1.5 K below the saturation temperature of steam at 40 bar.

$$T_l = 522 \, K \tag{4.10}$$

Along the tube surfaces, the heat flux entering the domain is set equal to that departing the tube side simulation.

$$\boldsymbol{q}_{total} = \boldsymbol{q}_{tubeSide} \tag{4.11}$$

This is achieved via a mapping functionality that exists within `OpenFOAM` which maps faces from different meshes to one another, weighting cell values by their overlapping areas. There is no heat flux through the tube sheet surface due to limitations of the mapping algorithm between simulations. This does not correspond to the tube side simulation though the surface is small compared to the tubes and heat flux is low at this point due to the insulating paper, hence the impact should be lessened.

$$\boldsymbol{n}_s \cdot \nabla T = 0 \, K/m \tag{4.12}$$

Both the shell bulk surface and the top outlet surface are governed by the same boundary condition. Similarly to flow, it is assumed that there is sufficient uniformity in flow properties as the simulation domain extends away from the high heat flux region at the end of the ferrule. Therefore, the gradient in temperature normal to the surface is set

to zero, implying constant properties from there on out. If viscous heating is negligible there should no longer be any source terms in the heat equation at this point as thermal energy only enters the system at the inlet and tube/tubesheet surfaces. While there is still thermal diffusion at the boundary, the effect is expected to be small, and of minor import to the results further upstream near the tubes which is this works primary interest.

$$\boldsymbol{n}_s \cdot \nabla T = 0 \; K/m \tag{4.13}$$

Finally, due to the periodic nature of the domain, the periodic surfaces are linked numerically.

Pure liquid water enters the system at the bottom surface such that:

$$\alpha_g = 0 \tag{4.14}$$

Similarly to other flow variables, it is assumed that the phase fraction becomes uniform as it approaches the shell bulk surface such that there is no gradient in α_g with respect to the surface normal. This condition is also applied to the top outlet of the simulation assuming that flow is fully developed at this point. Finally, due to numerical constraints imposed by the `OpenFOAM` finite volume package, the same boundary condition is applied to the solid surfaces to improve stability.

$$\boldsymbol{n}_s \cdot \nabla \alpha_g = 0 \; m^{-1} \tag{4.15}$$

The turbulent properties are specified with a Dirichlet boundary condition at the bottom inlet to the system. Similarly to the tube side simulations, k is determined by assuming that the energy associated with 5 percent of the velocity of the flow is turbulent. This corresponds to moderately turbulent flow, and is described in Eqn. (4.16):

$$k = \frac{3 \left\| \boldsymbol{V}_\infty \right\|^2 I^2}{2} = 3.75 \cdot 10^{-9} \; m^2/s^2 \tag{4.16}$$

where I is the turbulence intensity.

The turbulent dissipation rate at the inlet is determined from the turbulent kinetic energy inlet and a prescribed turbulent length scale. A length scale of 0.15 m was used in this simulation as it is the smallest repeating unit of geometry present.

$$\epsilon = C_\mu \frac{k_{inlet}^{\frac{3}{2}}}{l} = 1.38 \cdot 10^{-13} \; m^2/s^3 \tag{4.17}$$

where l is the turbulent length scale and C_μ is a turbulence model parameter, set to 0.09.

Similarly to other flow parameters, there is a Neumann condition applied to both the top outlet and shell bulk surfaces with the derivatives of the turbulent variables set to zero.

$$\boldsymbol{n}_s \cdot \nabla k_{l,g} = 0 \; m/s^2 \tag{4.18}$$

$$\boldsymbol{n}_s \cdot \nabla \epsilon_{l,g} = 0 \; m/s^3 \tag{4.19}$$

Finally, along the solid walls the turbulence variables are computed using standard $k-\epsilon$ wall function boundary conditions extended to multiphase flow [49].

$$k_{node} = \frac{\boldsymbol{V}_\tau^2}{\sqrt{C_\mu}} \; m/s^2 \tag{4.20}$$

$$\epsilon_{node} = \frac{k_{node}^{3/2} C_\mu^{3/4}}{K y_{node}} \; m^2/s^3 \tag{4.21}$$

where the subscript node means the value at the nearest cell centre to the wall, y_{node} is the distance of the node centre to the wall, and $K = 0.41$ is the van Karman constant.

The numerical package used to compute the shell side case was reactingTwoPhaseEuler-Foam. This solver is capable of solving the two fluid model, with additional phenomena such as species balances and reactions. The combination of limiter and discretization approach used in the shell side simulation was selected based on `OpenFOAM` guidelines [44] and is outlined below with further details available in section 2.7.

Variable	Discretization	Limiter
Velocity	LUD	linear
$\alpha_{l,g}$	CDS	VanLeer
Enthalpy	CDS	linear
Pressure	CDS	linear
k, ϵ	upwind	NA

Table 4.4: Numerical Approach Used for the Shell-Side Simulation

Care was taken when generating the mesh for this case as the reactingTwoPhaseEuler-Foam solver is known to be very sensitive to non-hexahedral and non-orthogonal meshes. The mesh consists of entirely structured hexahedral elements, the layout of which mimics the expected flow pattern. Having the mesh closely aligned with flow minimizes numerical errors by reducing the orthogonality corrector when calculating face fluxes between cells.
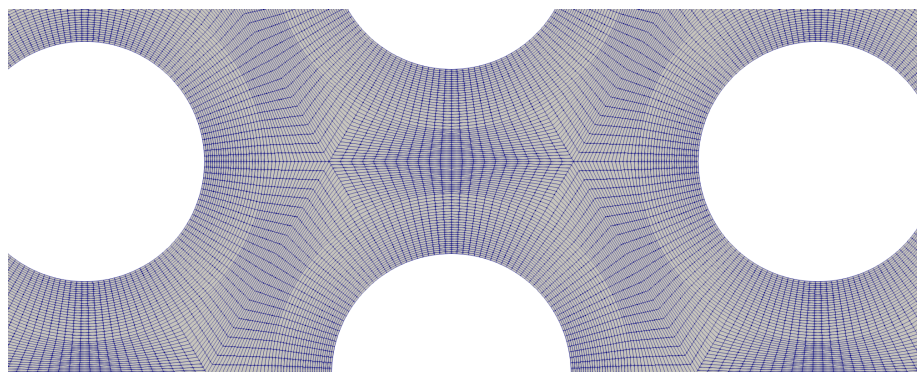
Figure 4.3: Mesh across the tubesheet face, note the fully structured highly orthogonal cells.

Unlike the tube side mesh there is little use of wall boundary layer elements in this domain. The purpose for this is twofold, first the two phase $k - \epsilon$ turbulence model for multi-phase flows is used in this simulation and being a ϵ based model the nearest cell region should fall within the log region of the boundary layer [50]. This is orders of magnitude more distant than the viscous sub-layer required for an ω equation. Second, due to the mismatch in boundary conditions at the tube surface (the liquid is no-slip while the gas is slip), having very tight boundary layers would be very constraining on the Courant number due to the presence of a relative velocity at the wall, leading to longer compute times.

4.3   Results Discussion

Using the configuration outlined above, the shell side simulation was run. The results are in line with expectations and industrial partner experience. As illustrated in Fig. 4.5 and Fig. 4.4, flow rises from the bottom of the domain to the top weaving through the tubes as it travels. The images were taken on a slice placed at the outlet of the ferrule, the region with the most intense boiling. Of particular interest is the impact that the phase change has on the flow profiles for both phases. The intense heat transfer at the outlet of the ferrule causes a peak in vapour generation along this length of tubing. The gravitational terms in Eqn. (2.43) and Eqn. (2.44) along with the density differences between the two phases in turn generates a buoyancy force on the vapour phase. Then as bubbles rise, the relative velocity between the phases manifests itself in the momentum drag term Eqn. (2.47) which accelerates the continuous liquid phase in part. This phenomena is visible in the liquid phase steam lines and velocity. In the case where liquid is the sole phase, when flowing
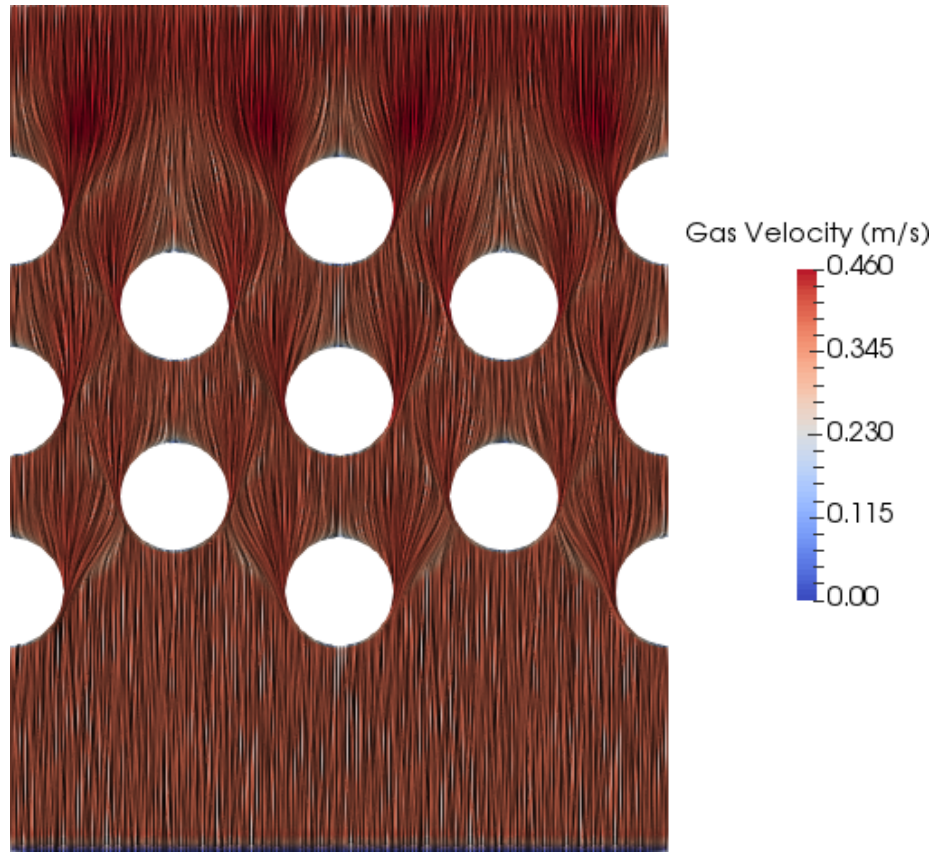
58

Figure 4.4: Lower speed flows are also pulled from the front of the tube sheet towards the high intensity boiling region.

past a bundle of tubes such as these, it is expected that velocities peak away from the tube walls due to the no slip boundary condition. Yet in this case it is clear that velocity peaks in close proximity to the tubes and furthermore rather than curve around the tubes, the stream lines curve towards the lower portion of each tube where the gaseous phase is most present.

Before encountering the tubes, the gas phase velocity is non-physical since there is no gas phase present. Hence outside of an initial acceleration to correct for buoyancy forces, there is no change in the gas velocity vector as it enters the domain. Once the tubes are reached though, there is gas phase production and the gas phase contours the tubes until approximately the 3 and 9 o'clock at which point the streamlines depict wall departure.

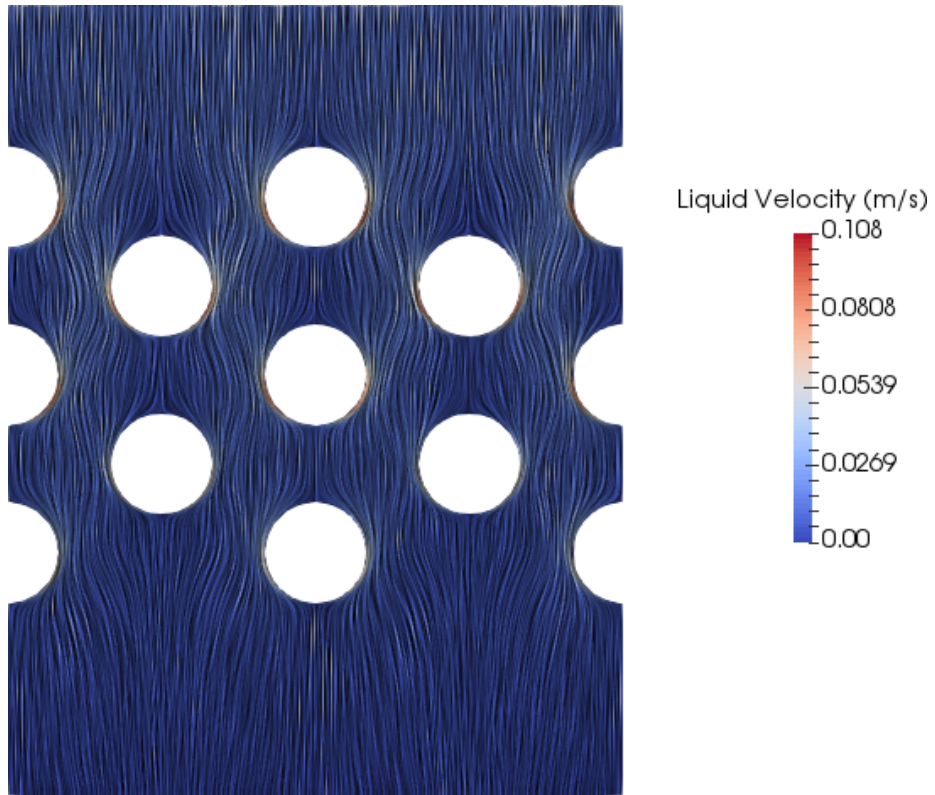Figure 4.6 and Fig. 4.7 further illustrate this effect, now along the z axis. Liquid fluid

Figure 4.5: Liquid velocity at the ferrule outlet overlayed with the liquid streamlines, notice the highest velocities occur near the edges of each tube due to vapour momentum exchange.
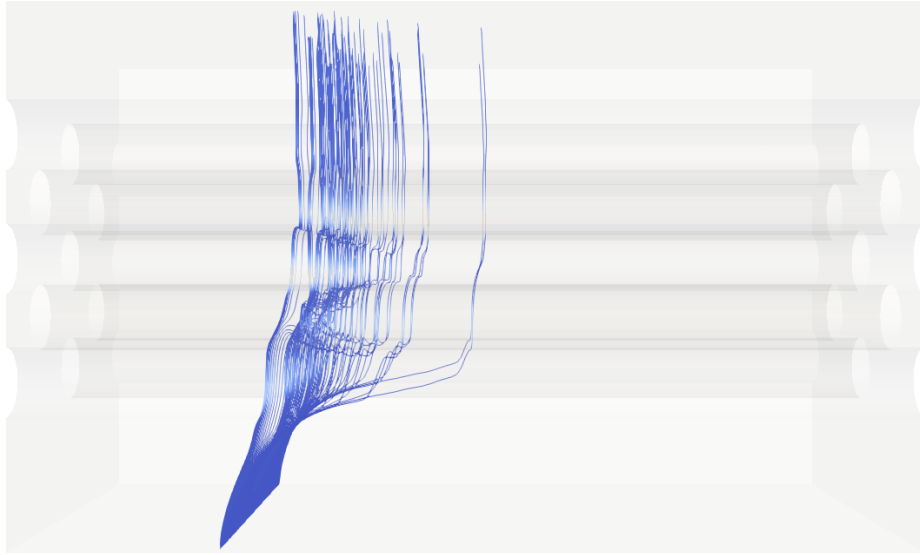
Figure 4.6: Stream lines following the path of liquid water illustrating how flow is driven by high intensity boiling and resulting buoyancy/drag forces at the outlet of the ferrule.

which enters the domain both before and after (when travelling along the tube length) the higher heat flux at the outlet of the ferrule is pulled towards this region due to the localized acceleration of the liquid phase. The effect is more pronounced in fluid entering directly underneath the tube portion insulated by the ferrule since very little vapour is generated here, and hence flow is relatively quiescent.

The pressure field follows the expected trend for this simulation. Mostly the pressure gradient is dictated by the hydro-static pressure of the liquid fluid. If this were a pure column of quiescent liquid water at these temperature conditions the pressure at the bottom surface would be 2979 Pa higher than at the top. Rather there is a difference of 2981 Pa meaning that only 2 Pa contributes to flow.

Also taken at the end of the ferrule, Fig. 4.9 reveals how the gaseous phase interacts with the solid walls. Due to buoyancy forces, all the gas generated along the bottom half of the tube rises and coalesces along the bottom surface of the tube. These bubbles then roll along the side of the tubes and disperse outward and upward near the 3 and 9 o'clock. This leads to high concentrations of gaseous phase along the bottom half of each tube, until the gas is able to rise and disperse. In contrast, the vapour generated on the upper halves of the tubes readily rises and disperses and therefore does not reach high concentrations.

Figure 4.10 is an image of the left side of the simulation, the tube surfaces being visible.
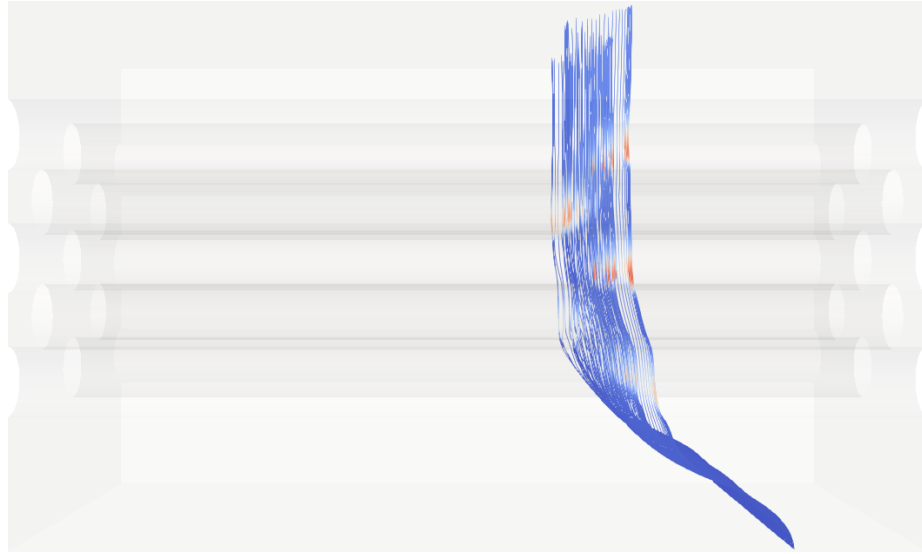
Figure 4.7: Again lower speed flows are also pulled from the front of the tube sheet towards the high intensity boiling region.
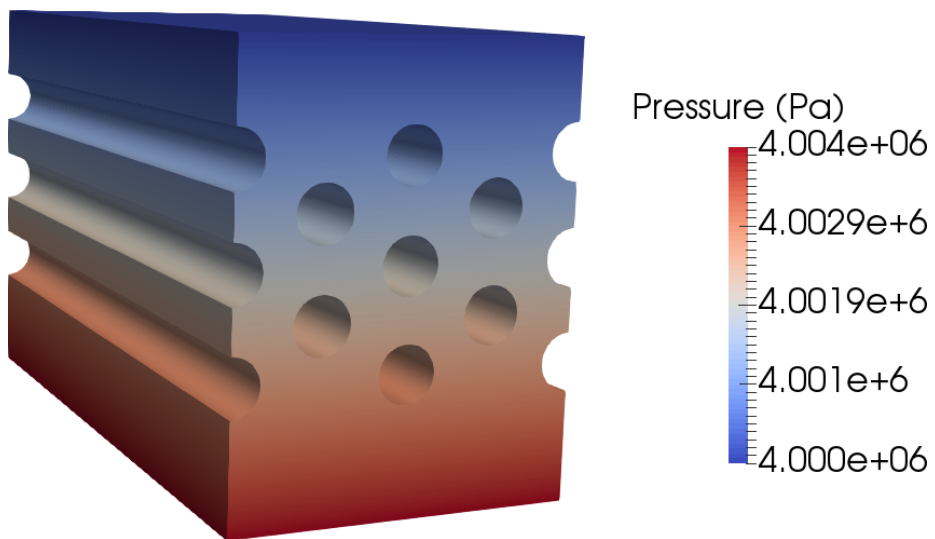

Figure 4.8: Pressure within shell side domain, mainly dominated by hydrostatic forces as visible via the constant gradient in pressure from top to bottom of the fluid domain.
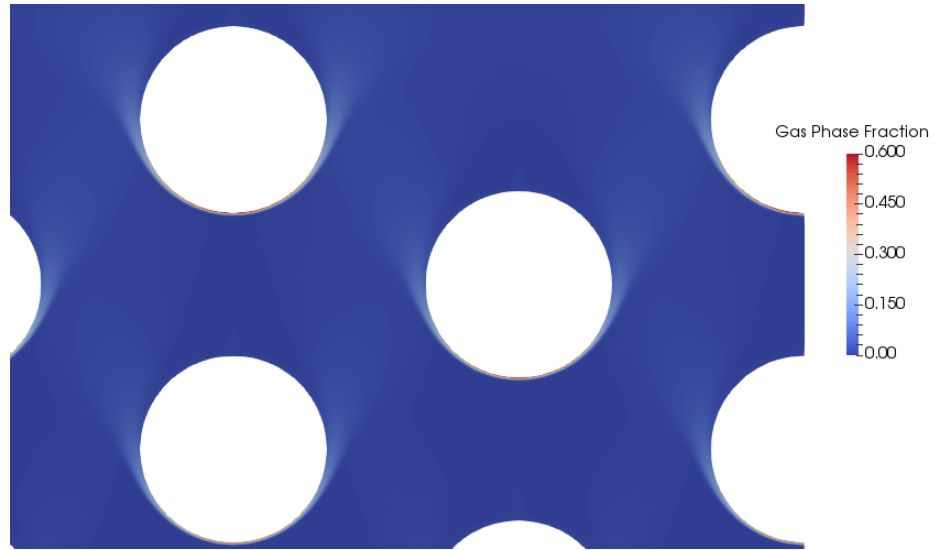
Figure 4.9: Vapour volume fraction at the outlet of the ferrules, outside of the bottom surface of tubes the vapour phase is very disperse through the simulation.
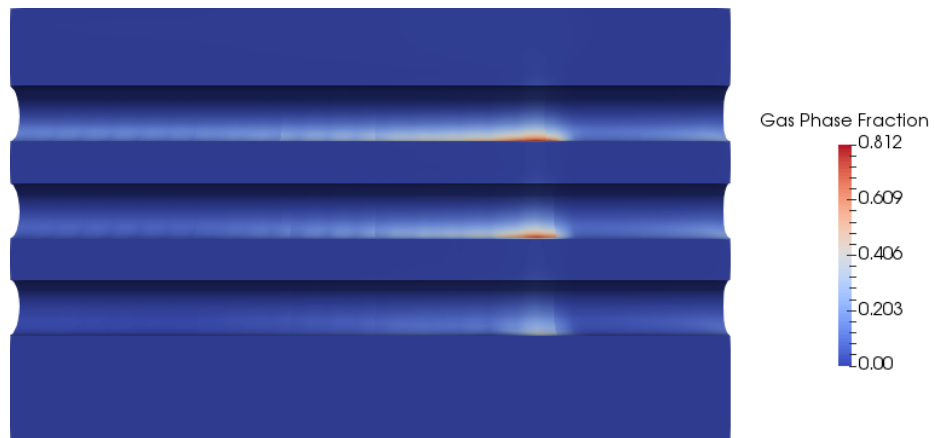

Figure 4.10: Gas coalesces at the bottom of each tube before rolling off the sides.

Of note is the rising concentration of vapour phase as the fluids rise, the reasons for this are two-fold. First, as flow rises some portion of dispersed vapour phase impinges on the tubes above the one it was generated on. This compounds with the higher vapour concentrations on the lower half of tubes due to buoyancy mentioned earlier to raise the phase fraction of gas even higher. Second, as the liquid rises it is also heated by the tubes, therefore when it encounters subsequent tubes the energy required to raise the liquid temperature to its boiling point is reduced and it boils more readily. Also visible in this figure is the increased boiling which occurs at the outlet of the ferrule. It is clear that the insulation to the metal tubes provided by the ferrule is effective in reducing the heat flux through this portion. Then there is an intense peak at the ferrule outlet in heat transfer and therefore boiling, which slowly peters off in the z-direction.

Figure 4.11 and Fig. 4.12 are isosurfaces of α_g at 10% and 30% respectively. They further illustrate the increased production of vapour near the ferrule outlet, and the increased gaseous phase presence as flow travels upwards through the domain. The increased liquid phase velocity near the tubes is also visible.

The temperature around the tube follows the expected trend of spiking near the ferrule outlet due to the recirculatory region. Temperature increases along the bottom surface of the tube, relative to the top, because the added phase fraction of gas reduces the local heat transfer coefficient. This effect is particularly pertinent as this should generates a θ (angle from the tubes 12 o'clock) variation to the heat flux through the tubes in further coupled simulations. As outlined in chapter 4 there is no θ dependency in the heat flux along the tubes outer surface, but through the coupling with the shell side simulation this will now be introduced to the tube side results.

There are some deficiencies with this simulation which impact its accuracy. First, as illustrated in the figures, the phase fraction of gas along the bottom surfaces exceeds 0.8. This raises two primary concerns; that it is possible that departure from nucleate boiling will have occurred at this point in the physical system, but as covered in section 2.5 the boiling model used assumes that the process is in the nucleate boiling regime. Also the elevated phase fraction of gas switches the gaseous phase from dispersed to continuous, which would require a reassignment of Eqn. (2.44) and Eqn. (2.43). This regime change only occurs in a very small band across the solid surfaces and elsewhere the gaseous phase is clearly dispersed, so this concern only pertains to a small section of the simulation.

Another deficiency is the inlet region, the impact of the intense boiling accelerating the liquid phase was more pronounced than expected and, as visible in Fig. 4.7, influences flow as soon as it enters the domain. This in conjunction with Eqn. (4.1) is possibly problematic since flow is likely constrained outside of its "natural" profile along this surface. Finally,
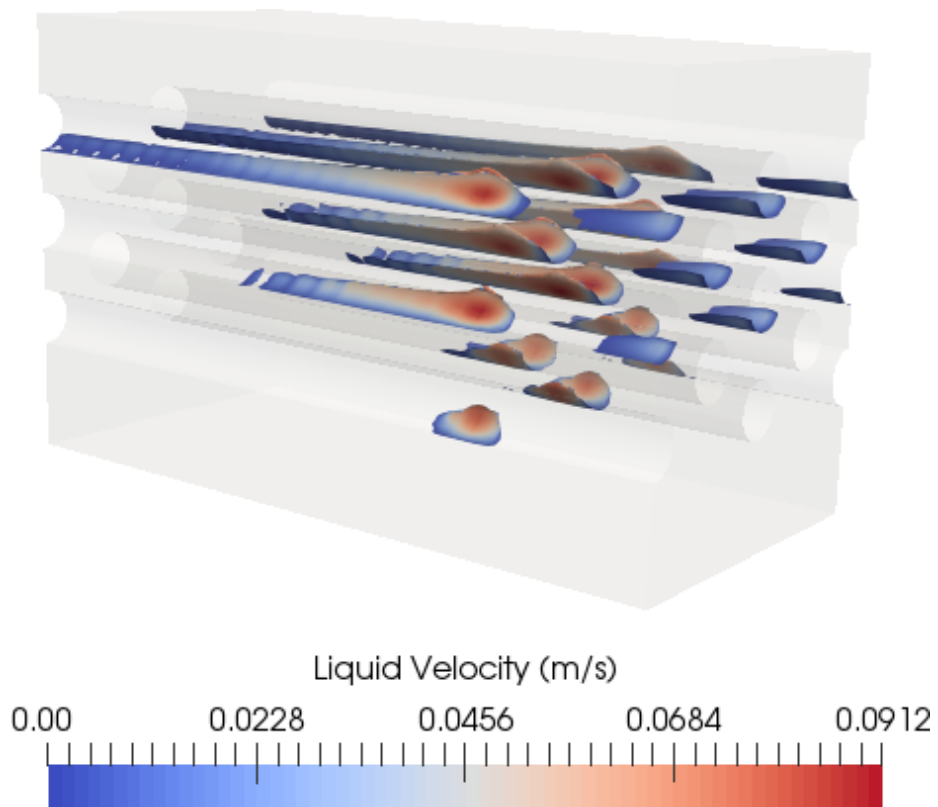
Figure 4.11: Surface representation of α_g at 10%, with a liquid velocity overlay. Notice how the highest liquid velocities occur near the largest concentration of gas.
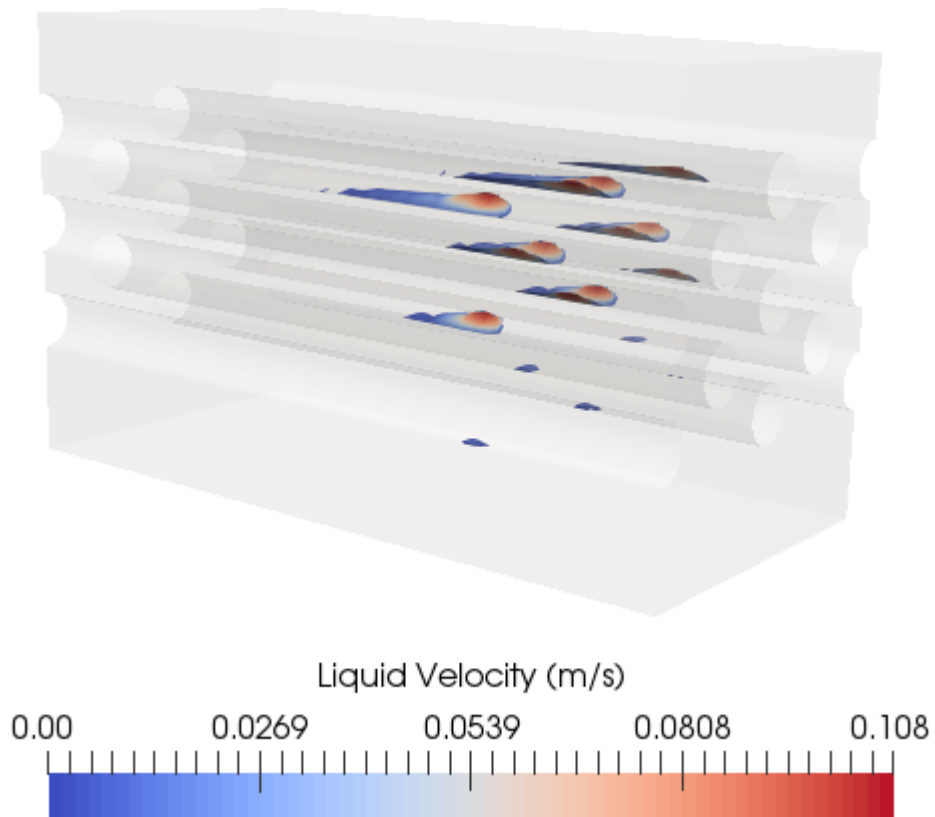
Figure 4.12: Surface representation of α_g at 30%, with a liquid velocity overlay. Steam generation occurs most vigorously at the exit of each ferrule in the recirculatory region
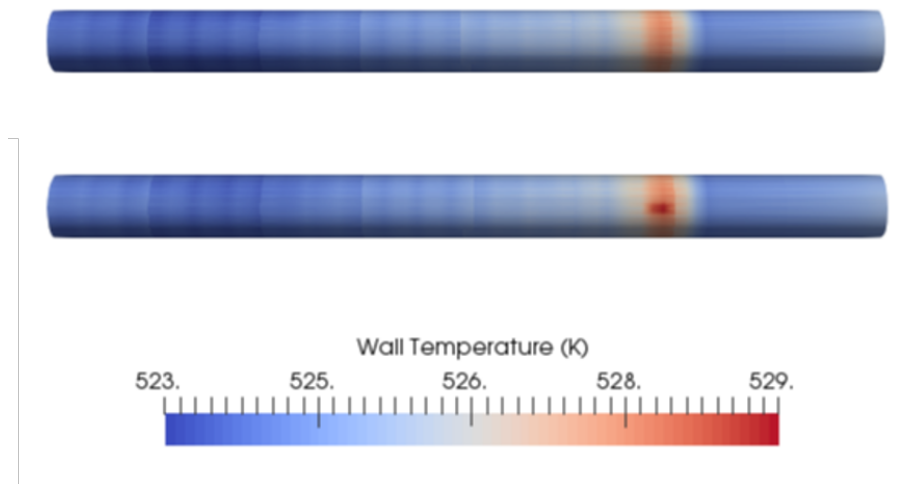
Figure 4.13: Top is the view from above, bottom is the view from below. Tube temperatures peak at the outlet of each ferrule before cooling again.

the mapping functionality between simulations could be improved, as visible in Fig. 4.13 the mapping between surfaces is not perfectly smooth and results in some cells receiving a portion of their neighbours heat flux.

Chapter 5

Coupled Model and Simulations

The operation of a waste heat boiler (WHB) is dependent on both the tube-side domain and shell-side domain as outlined in chapters 3 and 4, respectively. In order to achieve the best understanding possible of this complex system it is therefore necessary to consider both domains in context of their relationship to one another. Due to the numerical considerations previously mentioned, it is not possible to do so in a single numerical solve, rather solving both separately in an iterative manner with linked boundary conditions is a more feasible approach.

Coupling both sides was undertaken by first setting the heat flux output along the shared boundary of the tube-side simulation as a heat flux input to the shell-side simulation. After solving the shell-side with the updated heat flux, the temperature along the shared surface was set as the new boundary condition on the subsequent tube-side solve. The numerical solution to the updated tube-side was then computed and an iteration of the overall coupling completed.

As discussed earlier, the main objective of the insulating ferrule is to protect the metal of the WHB from corrosion which occurs at high temperatures and in the presence of hydrogen sulphide. The ferrule protects the metal by providing thermal insulation from the tube-side process gas, keeping the metal relatively cool. In consideration of this, the main metric of the ferrules performance is the metal temperature distribution. Maximum and minimum temperatures of the metal are also easy to compute in the tube-side solve hence they make a relevant and practical measurement of convergence for the coupling process.

The coupling process was performed 4 times at which point the change in maximum and minimum values was less than 0.1 %. Results for each run are summarized in table 5.1.

69

Iteration #	Maximum Metal Temperature (K)	% Change from Previous Iteration	Minimum Metal Temperature (K)	% Change from Previous Iteration
1	530.21	-	575.27	-
2	522.96	1.4%	548.48	4.8%
3	523.63	0.13%	546.07	0.44%
4	523.65	0.0038%	546.14	0.013%

Table 5.1: Coupling Key Parameter Results

As flow of the process gas in the tube-side was assumed to be independent of temperature as outlined in chapter 3, the flow variables in the coupled tube-side simulation remain unaltered from chapter 3 and, as such, the focus now will be on the metal temperatures. The metal domain is much cooler than in the uncoupled tube-side simulation. This implies that the assumed heat transfer coefficient used as the original boundary condition along the joined surface was significantly lower than is predicted by the shell-side simulation. Furthermore the liquid water at the inlet of the shell-side simulation is cooled a couple degrees below its boiling point, yet in the original tube-side simulation the bulk shell-side was assumed to be at the boiling temperature. While the coupled results predict lower metal temperatures, it is of note that the bundle of tubes modelled was of a limited size and the inlet to the shell-side simulation consisted only of liquid water and no vapour. This may not be indicative of an "average" tube within a WHB which is likely exposed to higher gas volume fractions and hence a lower heat transfer coefficient along its outer diameter.

The coupling of shell and tube-side allows for added insight into the operation of the WHB. Of note, the metal temperature distribution through the tube now varies with the angular co-ordinate. Along both the 6 and 12 o'clock of the tube, there is a notable peak in temperature. At the 12 o'clock this occurs because, as observed in the shell-side flow pattern, this is a stagnation point lowering the convective heat flux in the fluid phases. Meanwhile the hot spot along the 6 o'clock of each tube occurs due to a build up of water vapour at this point, since the vapour is less conductive than the liquid the temperature increases along the metal surface.

The coupling process does appear to have induced some smearing in the temperature profile along the outer radius of the tube. Likely this is due to the discrepancy in mesh resolution between shell and tube-side simulations. Both meshes have an equal number of nodes along the theta direction of the tube, but due to constraints on computational resources the shell-side mesh has one node for every four of the tube-side along the axial
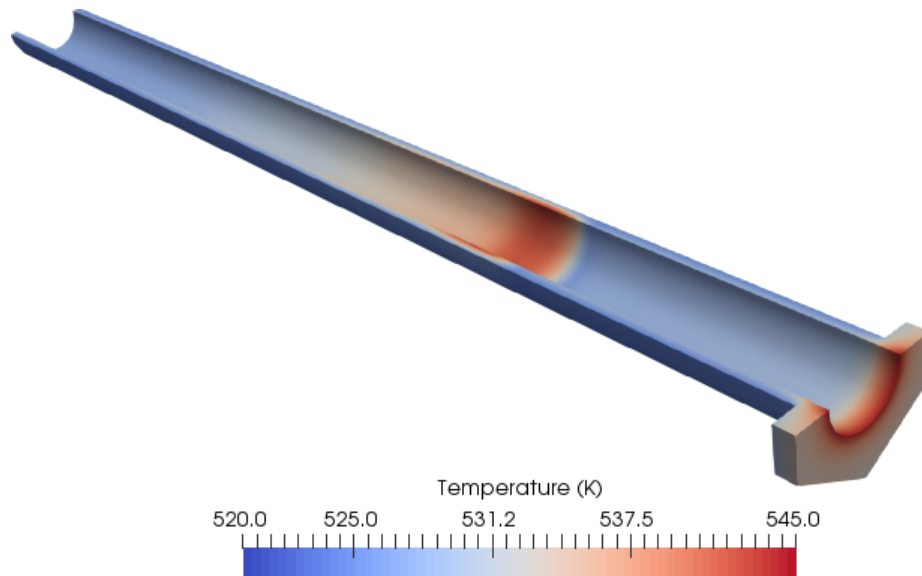
Figure 5.1: The cross sectional coupled simulation metal temperature profile demonstrates similar behaviour to the previous tube-side results but at cooler temperatures.
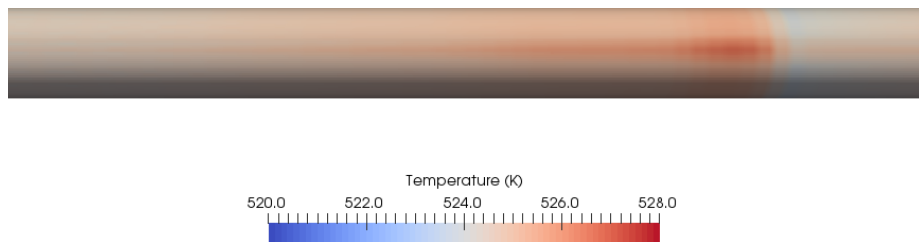

Figure 5.2: The view from above of the metal temperature demonstrates a clear theta dependency of the temperature profile.
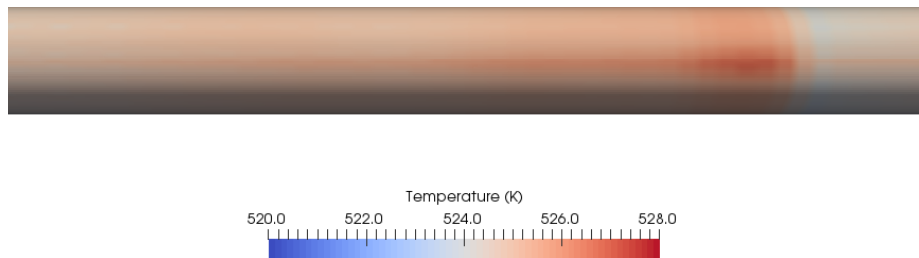

Figure 5.3: The view from below also has a temperature peak, and also shows the smearing of the temperature profile due to the mapping.
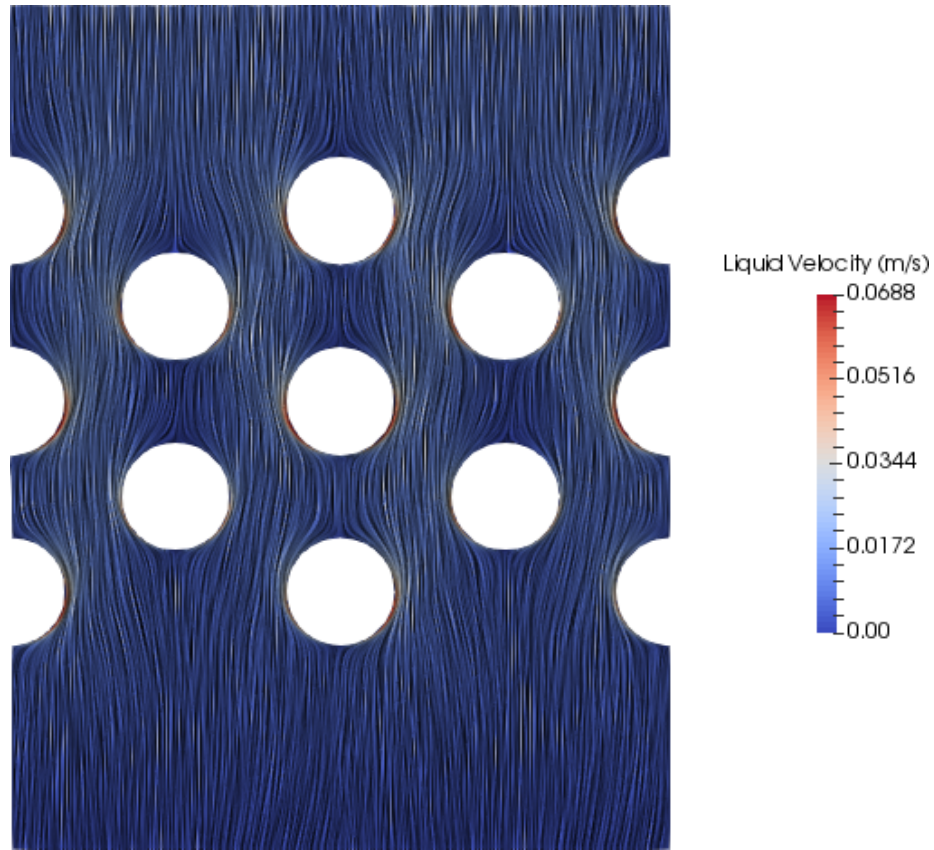
71

Figure 5.4: The liquid velocity also shows similar flow patterns to the original shell-side results, but is slightly slower due to lower vapour concentrations.

direction. Smearing is present particularly in this direction as the peak in temperature along the outer diameter, due to the recirculation zone at the end of the ferrule, is less pronounced than pre-coupling.

The shell-side results are mostly similar to the pre-coupling results, showing the same flow pattern of acceleration near the tube walls due to drag forces between the gas and liquid. Of note is a reduction in peak vapour concentrations and in the liquid velocities. Peak liquid velocities are lowered as a result of the lower peak gas phase concentrations, as there is less buoyancy and resulting drag, the liquid is not accelerated to the same degree. The heat flux through the tube surface and into the shell-side domain is largely unchanged as the temperature drop along the outer tube surface was accompanied by a commensurate drop along the internal surface in the tube-side simulation. As such a change in heat flux
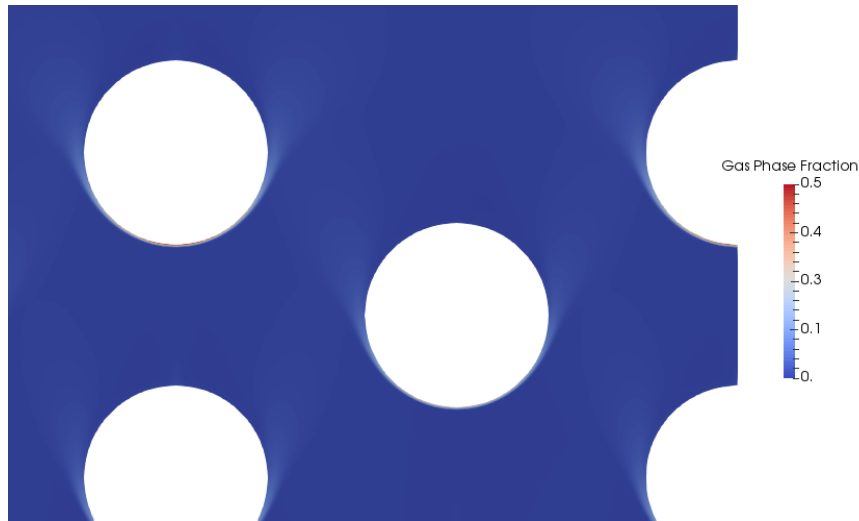
Figure 5.5: The phase fraction also is distributed similarly to the original shell-side simulation, but does not accumulate to the same degree on the underside of the tubes.

is not responsible for the drop in vapour phase. There are a few possible causes for the lessened vapour phase fraction along the tube surfaces, first there was a slight mesh change between the pre-coupling shell-side simulation and the coupled results.

As mentioned in the previous chapter there were some deficiencies in the mapping functionality provided by `OpenFOAM`, this was the result of a slight mis-match in cell sizes between the different simulations. With the original shell and tube-side simulations, for each shell-side element in along the axial direction there were approximately 4.1 tube-side elements. The heat flux mapping then assigned the entire heat flux of a tube-side element to a single shell-side element, resulting in some shell-side elements receiving the heat flux of 5 tube-side elements and others 4. This resulted in the "striped" appearance of Fig. 4.13, and after noting this, the tube-side mesh was adjusted to have 4 tube-side axial elements match 1 shell-side element exactly. Comparison of Fig. 5.6 and Fig. 5.7 illustrates the effects of the mesh adjustment as Fig. 5.6 is much smoother in the axial direction. The smoother profile has lower peaks in heat flux and therefore the corresponding production of vapour also has lesser peaks.

Another possible cause of lower vapour levels is the transient nature of the solve. The solver reactingTwoPhaseEulerFoam is a transient solver. When numerically solving the pre-coupled shell-side results the solution appeared to have reached a steady state after 2 seconds of simulation time after heat transfer had been initiated (the flow profile and
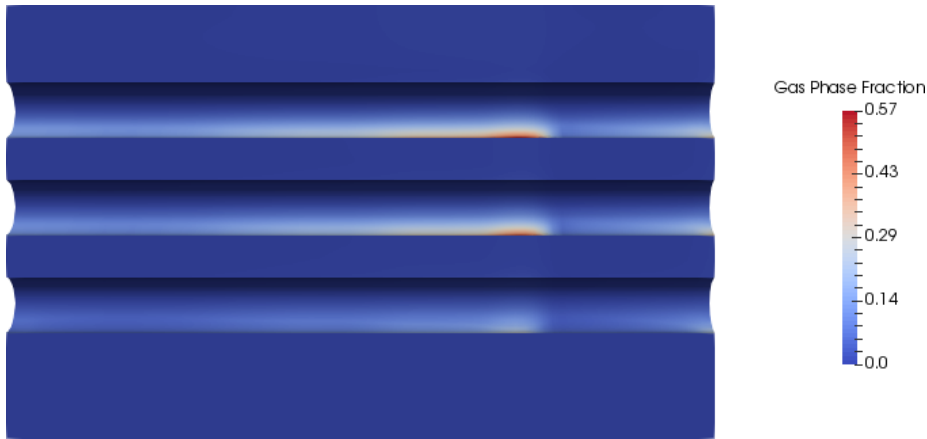
Figure 5.6: The phase fraction along the periodic boundary is much smoother compared to the original shell-side simulation due to improvements in mesh mapping.
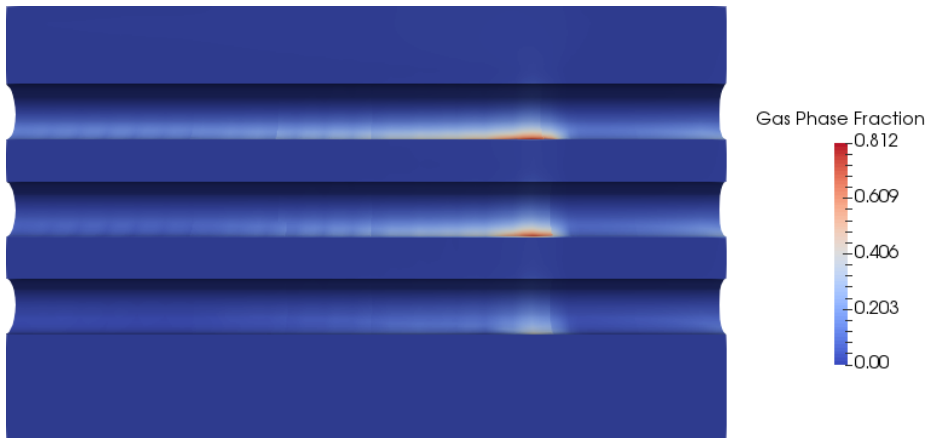

Figure 5.7: Notice the jaggedness of phase fraction in the original shell-side simulation.

pressure distribution for just the liquid phase flow had been computed previously). The results in chapter 4 are from this point in time. However it must be noted that this assumption was not thoroughly proven through a longer time frame. In the coupling algorithm the results from the previous iteration were used as a starting point for the solution, the only change between iterations being the heat flux boundary condition along the tubes. Each iteration was allowed to run for the 2 seconds of simulation time required to reach pseudo steady state in the first solve, such that by the final iteration the simulation had run for 10 seconds of simulation time albeit with a changing heat flux boundary condition. It is possible that, given more simulation time, the original shell-side simulation would have more closely resembled the results post-coupling.

In conclusion the coupling process provided additional insight into the operation of a WHB and operation of the ferrule system. An additional dimensional variation of the temperature distribution in the metal tubes was observed due to the shell-side physics. Concerns due to the transient nature of the solve and mesh sizing discrepancy between the two simulation domains were presented in this chapter. The coupling process provides valuable insight and could be extended to further improve the design and understanding of WHB operations.

Chapter 6

Conclusions and Future Work

6.1 Conclusion

In this work, continuum multiphysics models for both shell and tube side of a WHB are developed and simulated using decoupled and coupled methods. An iterative coupling method for the determination of the steady-state numerical solution to these models is then used to simulate a sub-region of a typical WHB.

The outlet geometry of the ferrule was found to significantly effect fluid flow and heat transfer in this region leading to a localized hot spot at the end of the recirculation zone. Simulation results were compared to empirical correlations typically used in the design of these units and significant deviation was found due to these localized effects. The predicted flow characteristics are relatively complex and it is expected that simulation results provide more accurate insight into actual performance of the WHB.

Simulations of the shell-side of the WHB involved the use of a multiphase model and mechanistic boiling model. While simulation results are promising, they are currently valid only for qualitative assessment of the interplay between convection far from the tubes and boiling on the surface of the tubes. Strong coupling was found between the buoyancy and drag forces in the near vicinity of tube surfaces and the flow profile of the two phases. Furthermore, insulating effects of the gaseous phase were found to lead to localized hot spots along the tube surface, imparting an angular variation in the metal temperature distribution.

Preliminary results for the coupling of both simulations was presented and resulted in lower metal temperatures than originally predicted in the single tube side simulation. As

a proof-of-concept, coupling with the conductive transport from the tube side simulations is a promising approach for truly comprehensive WHB simulations in the future.

6.2   Future Work

- Improvement of the tube side simulations, particularly by considering compressible flow and variable physical properties. There are large changes in temperature and pressure such that the density of the fluid along with physical properties of solids and fluid (thermal conductivity, specific heat, ect.) are not constant within the range of temperatures and pressures present in this system.

- Improvement of the shell side simulations through a more accurate boiling model and larger domain. The boiling model used is practical for its ease of implementation and closures, but relies heavily on empirical correlations and closures which may not be valid for all flow regimes and pressures. Also the shell side exhibits complex flow patterns, dependent on location with in shell, placement of boiler water inlets, and wall effects. To better represent the shell side a full simulation of a boiler should be resolved numerically.

- Further work on fully coupled simulations, particularly the mapping process. Using fully paired meshes would be ideal to avoid loss of information during the mapping process. Also the mapping functionality in-built into `OpenFOAM` could be improved upon to better map the heat flux between simulations, though this should be mitigated via paired meshes. These works should be used for the rational design and optimization of WHBs and heat exchangers in which phase change occurs.

APPENDICES

Appendix 1

Term	FvScheme
∇f	Gauss linear
$\nabla \cdot u$	bounded Gauss limitedLinear 1
$\nabla \cdot k$	bounded Gauss limitedLinear 1
$\nabla \cdot \omega$	bounded Gauss limitedLinear 1
$\nabla \cdot h$	bounded Gauss limitedLinear 1

Table A1: Finite Volume Discretization Scheme Applied in `OpenFOAM` for Tube-Side Simulation

Variable	Inlet	Outlet	Walls	Symmetric
Velocity (m/s)	fixedValue (0 0 -12)	zeroGradient	noSlip	slip
Pressure (kPa)	fixedFluxPressure	fixedValue 101.3	zeroGradient	zeroGradient
Turbulent Kinetic Energy (m^2/s^2)	turbulentInesity-KineticEnergy-Inlet 0.05	zeroGradient	fixedValue 0	zeroGraident
Specific Rate of Dissipation (1/s)	fixedValue	zeroGradient	omegaWallFunction	fixedValue 2
Temperature (K)	fixedValue 1400	zeroGradient	compressible::turbulentTemperatureCoupled-BaffleMixed	zeroGradient

Table A2: Boundary Conditions for Fluid Phase Tube Side Simulation

Term	FvScheme
$\frac{\delta f}{\delta t}$	CrankNicolson 0.5
∇f	cellMDLimited Gauss linear 0.5
$\nabla \cdot u$	Gauss linearUpwind grad(U)
$\nabla \cdot k$	Gauss upwind
$\nabla \cdot \epsilon$	Gauss upwind
$\nabla \cdot h$	Gauss limitedLinear 1
$\nabla \cdot p$	Gauss limitedLinear 1
$\nabla \cdot \alpha$	Gauss vanLeer01

Table A3: Finite Volume Discretization Scheme Applied in `OpenFOAM` for Shell-Side Simulation

Variable	Inlet	Outlet	Walls	Rear	Periodic
Velocity Liquid (mm/s)	fixedValue (0 0.9 0)	zeroGradient	noSlip	slip	cyclic
Velocity Gas (mm/s)	fixedValue (0 0.9 0)	zeroGradient	slip	slip	cyclic
Pressure (kPa)	fixedFlux-Pressure	prghPressure 4000	zeroGradient	zeroGradient	cyclic
Turbulent Kinetic Energy (m^2/s^2)	turbulentInesityKineticEnergy-Inlet 0.05	zeroGradient	kqRWall-Function	zeroGraident	cyclic
Rate of Dissipation (m^2/s^3)	fixedValue 1.38e-13	zeroGradient	epsilonWallFunction	zeroGradient	cyclic
Temperature (K)	fixedValue 522	zeroGradient	fixedMulti-PhaseHeat-Flux	zeroGradient	cyclic
Gas Phase Fraction	fixedValue 0	zeroGradient	zeroGraident	zeroGradient	cyclic

Table A4: Boundary Conditions for Shell Side Simulation

Appendix 2

Consider the heat equation for an incompressible fluid assuming independence of the y and z directions:

$$\rho C_v \left(\frac{\partial T}{\partial t} + \boldsymbol{V}_x \frac{\delta T}{\delta x} \right) = k \frac{\delta^2 T}{\delta x^2} + 2\mu \left(\frac{\delta \boldsymbol{V}_x}{\delta x} \right)^2 + \mu \left[\left(\frac{\delta \boldsymbol{V}_y}{\delta x} \right)^2 + \left(\frac{\delta \boldsymbol{V}_z}{\delta x} \right)^2 \right] \tag{1}$$

let:

$$x = lx' \tag{2}$$

$$\boldsymbol{V}_x = V_\circ \boldsymbol{V}_x' \tag{3}$$

$$\boldsymbol{V}_y = V_\circ \boldsymbol{V}_y' \tag{4}$$

$$\boldsymbol{V}_z = V_\circ \boldsymbol{V}_z' \tag{5}$$

$$T = T_\circ + \Delta T \, T' \tag{6}$$

$$t = \frac{l}{V_\circ} t' \tag{7}$$

where l, $V_\circ$, and ΔT are the characteristic length, velocity, and temperature change in the system.

After some rearrangement using chain rule:

$$\frac{\partial T'}{\partial t'} + \boldsymbol{V}_x \frac{\delta T'}{\delta x'} = \frac{k}{\rho C_v l V_\circ} \frac{\delta^2 T'}{\delta x'^2} + \frac{2\mu V_\circ}{\rho C_v l \Delta T} \left(\frac{\delta \boldsymbol{V}_x}{\delta x} \right)^2 + \frac{\mu V_\circ}{\rho C_v l \Delta T} \left[\left(\frac{\delta \boldsymbol{V}_y}{\delta x} \right)^2 + \left(\frac{\delta \boldsymbol{V}_z}{\delta x} \right)^2 \right] \tag{8}$$

For a typical ferrule system let: $l = 0.03\,m$, $V_\circ = 10\,m/s$, and $\Delta T = 100\,^\circ K$. In this case:

$$\frac{\partial T'}{\partial t'} + \boldsymbol{V}_x \frac{\delta T'}{\delta x'} = 7.13 \cdot 10^{-5} \frac{\delta^2 T'}{\delta x'^2} + 8.22 \cdot 10^{-8} \left(\frac{\delta \boldsymbol{V}_x}{\delta x} \right)^2 + 4.11 \cdot 10^{-8} \left[\left(\frac{\delta \boldsymbol{V}_y}{\delta x} \right)^2 + \left(\frac{\delta \boldsymbol{V}_z}{\delta x} \right)^2 \right] \tag{9}$$

As the viscous generation terms are $<< 1$ the governing equation may be simplified to that presented in Eqn. (2.5) repeated below:

$$\rho C_v \left(\frac{\partial T}{\partial t} + \boldsymbol{V} \cdot \nabla T \right) = k \nabla^2 T \tag{10}$$

References

[1] Enviroment Canada. Canadian smog science assessment highlights and key messages, 2019 (accessed June 25, 2019). URL http://www.ec.gc.ca/air/default.asp?lang=En&n=72F82C27-1&offset=7#toc7-3.

[2] Enersul. Sulphur block pouring, 2019 (accessed June 25, 2019). URL https://www.enersul.com/sulphur-solutions/sulphur-block-pouring/.

[3] Alberta Energy Regulator. Sulphur supply/demand, 2019 (accessed June 25, 2019). URL https://www.aer.ca/providing-information/data-and-reports/statistical-reports/sulphur-supply-demand.

[4] Hideki Kurimura, Gary T. Rochelle, and Kamy Sepehrnoori. An expert system to select acid gas treating processes for natural gas processing plants. *Gas Separation and Purification*, 7(3):151 – 158, 1993. ISSN 0950-4214. doi: https://doi.org/10.1016/0950-4214(93)80004-G. URL http://www.sciencedirect.com/science/article/pii/095042149380004G.

[5] National Energy Technology Laboratory US Department of Energy. The claus process, 2019 (accessed June 25, 2019). URL https://netl.doe.gov/research/coal/energy-systems/gasification/gasifipedia/claus-process.

[6] James R Welty, Charles E Wicks, Gregory Rorrer, and Robert E Wilson. *Fundamentals of momentum, heat, and mass transfer*. John Wiley & Sons, 2009.

[7] U.S. Energy Information Administration Office of Energy Analysis. *Annual Energy Outlook 2019*. U.S. Department of Energy, 2009.

[8] Dupont. Clean technologies, 2019 (accessed June 25, 2019). URL http://cleantechnologies.dupont.com/technologies/mecs/mecsr-zecorr-alloys-sulfuric-acid-plant-equipment/mecsr-process-critical-equipment/mecsr-hexprotm-ferrules/.

[9] Henk Kaarle Versteeg and Weeratunge Malalasekera. *An introduction to computational fluid dynamics: the finite volume method*. Pearson education, 2007.

[10] R Byron Bird, Warren E Stewart, and Edwin N Lightfoot. *Transport phenomena*. John Wiley & Sons, 2007.

[11] W.D. McComb. *The physics of fluid turbulence*. Oxford Science Publications, 1990.

[12] Reactor Physics. Laminar flow vs. turbulent flow, 2019 (accessed June 25, 2019). URL https://www.reactor-physics.com/engineering/fluid-dynamics/laminar-flow-vs-turbulent-flow/.

[13] Tom E Faber. *Fluid dynamics for physicists*. Cambridge university press, 1995.

[14] M. T. Landahl and E. Mollo-Christensen. *Turbulence and Random Processes in Fluid Mechanics*. Cambridge University Press, 2 edition, 1992. doi: 10.1017/9781139174008.

[15] Lars Davidson. Fluid mechanics, turbulent flow and turbulence modeling, 2015.

[16] Edward A Spiegel and G Veronis. On the boussinesq approximation for a compressible fluid. *The Astrophysical Journal*, 131:442, 1960.

[17] Stuart W. Churchill. A reinterpretation of the turbulent prandtl number. *Industrial & Engineering Chemistry Research*, 41(25):6393–6401, 2002. doi: 10.1021/ie011021k. URL https://doi.org/10.1021/ie011021k.

[18] Joel H Ferziger and Milovan Peric. *Computational methods for fluid dynamics*. Springer Science & Business Media, 2012.

[19] Florian R Menter. Two-equation eddy-viscosity turbulence models for engineering applications. *AIAA journal*, 32(8):1598–1605, 1994.

[20] Tanyakarn Treeratanaphitak. *Diffuse Solid/Multi-Fluid Interface Method for Dispersed Multiphase Flows*. PhD thesis, University of Waterloo, 2018.

[21] Mamoru Ishii and Takashi Hibiki. *Thermo-fluid dynamics of two-phase flow*. Springer Science & Business Media, 2010.

[22] Donald A Drew. Mathematical modeling of two-phase flow. *Annual review of fluid mechanics*, 15(1):261–291, 1983.

[23] WE Ranz, W R_ Marshall, et al. Evaporation from drops. *Chem. Eng. Prog*, 48(3): 141–146, 1952.

[24] Shiro Nukiyama. The maximum and minimum values of the heat q transmitted from metal to boiling water under atmospheric pressure. *International Journal of Heat and Mass Transfer*, 9(12):1419 – 1433, 1966. ISSN 0017-9310. doi: https://doi.org/10.1016/0017-9310(66)90138-4. URL http://www.sciencedirect.com/science/article/pii/0017931066901384.

[25] Engineers Edge. Water boiling graph curve at 1 atmosphere, 2019 (accessed June 25, 2019). URL https://www.engineersedge.com/heat_transfer/water_boiling_graph_curve_13825.htm.

[26] Jungho Kim. Review of nucleate pool boiling bubble heat transfer mechanisms. *International Journal of Multiphase Flow*, 35(12):1067 – 1076, 2009. ISSN 0301-9322. doi: https://doi.org/10.1016/j.ijmultiphaseflow.2009.07.008. URL http://www.sciencedirect.com/science/article/pii/S0301932209001311.

[27] S.F. Jones, G.M. Evans, and K.P. Galvin. Bubble nucleation from gas cavities a review. *Advances in Colloid and Interface Science*, 80(1):27 – 50, 1999. ISSN 0001-8686. doi: https://doi.org/10.1016/S0001-8686(98)00074-8. URL http://www.sciencedirect.com/science/article/pii/S0001868698000748.

[28] K Engleberg-Forster and R Grief. Heat transfer to a boiling liquid-mechanisms and correlations'. *Trans ASME J of Heat Transfer, 81c*, 43, 1959.

[29] Chi-Yeh Han. *The mechanism of heat transfer in nucleate pool boiling*. PhD thesis, Massachusetts Institute of Technology, 1962.

[30] BB Mikic and WM Rohsenow. A new correlation of pool-boiling data including the effect of heating surface characteristics. *Journal of Heat Transfer*, 91(2):245–250, 1969.

[31] M.G. Cooper and A.J.P. Lloyd. The microlayer in nucleate pool boiling. *International Journal of Heat and Mass Transfer*, 12(8):895 – 913, 1969. ISSN 0017-9310. doi: https://doi.org/10.1016/0017-9310(69)90154-9. URL http://www.sciencedirect.com/science/article/pii/0017931069901549.

[32] P. Stephan and J. Hammer. A new model for nucleate boiling heat transfer. *Heat and Mass Transfer*, 30(2):119–125, Nov 1994. ISSN 1432-1181. doi: 10.1007/BF00715018. URL https://doi.org/10.1007/BF00715018.

[33] Masahiro Shoji. Studies of boiling chaos: a review. *International Journal of Heat and Mass Transfer*, 47(6):1105 – 1128, 2004. ISSN 0017-9310. doi: https://doi.org/

10.1016/j.ijheatmasstransfer.2003.09.024. URL http://www.sciencedirect.com/science/article/pii/S0017931003005635.

[34] D.B.R. Kenning. Wall temperature patterns in nucleate boiling. *International Journal of Heat and Mass Transfer*, 35(1):73 – 86, 1992. ISSN 0017-9310. doi: https://doi.org/10.1016/0017-9310(92)90009-H. URL http://www.sciencedirect.com/science/article/pii/001793109290009H.

[35] N Kurul and M.Z. Podowski. On the modeling of multidimensional effects in boiling channels. *ANS. Proc. National Heat Transfer Con. Minneapolis, Minnesota, USA, 1991*, 1991.

[36] Victor H. Del Valle and D.B.R. Kenning. Subcooled flow boiling at high heat flux. *International Journal of Heat and Mass Transfer*, 28(10):1907 – 1920, 1985. ISSN 0017-9310. doi: https://doi.org/10.1016/0017-9310(85)90213-3. URL http://www.sciencedirect.com/science/article/pii/0017931085902133.

[37] Robert Cole. A photographic study of pool boiling in the region of the critical heat flux. *AIChE Journal*, 6(4):533–538, 1960.

[38] VI Tolubinsky and DM Kostanchuk. Vapour bubbles growth rate and heat transfer intensity at subcooled water boiling. In *International Heat Transfer Conference 4*, volume 23. Begel House Inc., 1970.

[39] M Lemmert and JM Chawla. Influence of flow velocity on surface boiling heat transfer coefficient. *Heat Transfer in Boiling*, 237:247, 1977.

[40] Huaishuang Shao, Qinxin Zhao, Zhiyuan Liang, and Yungang Wang. Numerical investigation on a separated structure shell-and-tube waste heat boiler based on experiment. *International Journal of Heat and Mass Transfer*, 117:1006 – 1018, 2018. ISSN 0017-9310. doi: https://doi.org/10.1016/j.ijheatmasstransfer.2017.09.127. URL http://www.sciencedirect.com/science/article/pii/S0017931017316307.

[41] Junjie Ji, Yuling Shi, and Chunlu Zhang. Hybrid numerical simulation of large-scale gas-fired tubular heat exchangers. *HVAC&R Research*, 17(1):118–130, 2011. doi: 10.1080/10789669.2011.543257. URL https://www.tandfonline.com/doi/abs/10.1080/10789669.2011.543257.

[42] Baozhi Sun and Yuanlong Yang. Numerically investigating the influence of tube support plates on thermal-hydraulic characteristics in a steam generator. *Applied Thermal Engineering*, 51(1):611 – 622, 2013. ISSN 1359-4311. doi: https://doi.

org/10.1016/j.applthermaleng.2012.10.009. URL http://www.sciencedirect.com/science/article/pii/S1359431112006655.

[43] Chenglong Wang, Tenglong Cong, Suizheng Qiu, Wenxi Tian, Yingwei Wu, and Guanghui Su. Numerical prediction of subcooled wall boiling in the secondary side of sg tubes coupled with primary coolant. *Annals of Nuclear Energy*, 63:633 – 645, 2014. ISSN 0306-4549. doi: https://doi.org/10.1016/j.anucene.2013.09.006. URL http://www.sciencedirect.com/science/article/pii/S0306454913004763.

[44] The OpenFOAM Foundation. Openfoam v6 user guide, 2017. URL https://cfd.direct/openfoam/user-guide.

[45] Bram van Leer. Towards the ultimate conservative difference scheme. ii. monotonicity and conservation combined in a second-order scheme. *Journal of Computational Physics*, 14(4):361 – 370, 1974. ISSN 0021-9991. doi: https://doi.org/10.1016/0021-9991(74)90019-9. URL http://www.sciencedirect.com/science/article/pii/0021999174900199.

[46] Geoffrey Frederick Hewitt, George L Shires, and Theodore Reginald Bott. *Process heat transfer*, volume 113. CRC press Boca Raton, FL, 1994.

[47] National Aeronautics and Space Administration. Langley research center turbulence modeling resource, 2019 (accessed June 25, 2019). URL https://turbmodels.larc.nasa.gov/.

[48] Hiroto SAKASHITA. Bubble growth rates and nucleation site densities in saturated pool boiling of water at high pressures. *Journal of Nuclear Science and Technology*, 48(5):734–743, 2011. doi: 10.1080/18811248.2011.9711756.

[49] Jonas Bredberg. *On the Wall Boundary Condition for Turbulence Models*. Department of Thermo and Fluid Dynamics Chalmers University of Technology, 2000.

[50] Richard T. Lahey. The simulation of multidimensional multiphase flows. *Nuclear Engineering and Design*, 235(10):1043 – 1060, 2005. ISSN 0029-5493. doi: https://doi.org/10.1016/j.nucengdes.2005.02.020. URL http://www.sciencedirect.com/science/article/pii/S0029549305000798. Festschrift Edition Celebrating the 65th Birthday of Prof. Richard T. Lahey, Jr.